Acta Mech 202, 181–204 (2009)
DOI 10.1007/s00707-008-0018-6

O. A. Bég · J. Zueco · T. A. Bég · H. S. Takhar · E. Kahya

NSM analysis of time-dependent nonlinear buoyancy-driven double-diffusive radiative convection flow in non-Darcy geological porous media

Received: 14 December 2007 / Revised: 14 February 2008 / Published online: 13 June 2008

Abstract A network numerical simulator is developed and described to simulate the transient, nonlinear buoyancy-driven double diffusive heat and mass transfer of a viscous, incompressible, gray, absorbing–emitting fluid flowing past an impulsively started moving vertical plate adjacent to a non-Darcian geological porous regime. The governing boundary-layer equations are formulated in an (X^*, Y^*, t^*) coordinate system with appropriate boundary conditions. An algebraic diffusion approximation is used to simplify the radiation heat transfer contribution. The non-dimensionalized transport equations are solved in an (X, Y, t) coordinate system using the network simulation model (NSM) and the computer code, Pspice. A detailed discussion of the network design is provided. The effects of Prandtl number, radiation–conduction parameter (Stark number), thermal Grashof number, species Grashof number, Schmidt number, Darcy number and Forchheimer number on the transient dimensionless velocities (U, V), non-dimensional temperature (T) and dimensionless concentration function (C) are illustrated graphically. Additionally, we have computed plots of U, V, T, C versus time and average Nusselt number and Sherwood number versus X, Y coordinate, for various thermophysical parameters. The model finds applications in geological contamination, geothermal energy systems and radioactive waste-repository near-field thermo-geofluid mechanics.

O. A. Bég (✉)
Aerodynamics Group, Aerosciences Program, Academic Wing, BAE Systems, Riyadh 11441, Kingdom of Saudi Arabia
E-mail: docoanwarbeg@hotmail.co.uk

J. Zueco
Departamento de Ingeniería Térmica y Fluidos, ETS Ingenieros Industriales, Universidad Politécnica de Cartagena, Campus Muralla del Mar, Cartagena, Murcia 30203, Spain
E-mail: joaquin.zueco@upct.es

T. A. Bég
Engineering Mechanics and Seismic Dynamics Research, 18 Milton Grove, Manchester M16 OBP, UK
E-mail: A.Beg@email.com

H. S. Takhar
Engineering Department, Manchester Metropolitan University, Manchester M15GD, UK
E-mail: h.s.takhar@mmu.ac.uk

E. Kahya
Hydrology, Water Resources and Hydraulics Program, Civil Engineering Department, Istanbul Technical University, Ayazaga, Istanbul 34469, Turkey
E-mail: kahyae@itu.edu.tr

Present Address:
O. A. Bég
Civil Engineering Program, R-Block, Castle College, Granville Road, Sheffield S22RL, UK

1 Introduction

Computational transport modelling of buoyancy-induced (i.e. natural convection) flows in geomaterials is of considerable interest in environmental and civil engineering sciences. Numerous applications exist of such flows. Environmental transport processes in soils [1], forest fire development through brush and dry soils [2], geothermal processes [3], radioactive waste storage [4] and thermal plumes in magmatic geosystems constitute just a few important applications of geological thermofluid transport modelling. A thorough discussion of these and other applications is available in the monographs by Ingham and Pop [5] and Nield and Bejan [6]. Many techniques have been developed to simulate these and other double-diffusive convection flows including finite element techniques [7], finite difference solvers [8], spectral element methods, finite volume solvers, etc. Ligget and Liu [9] used the boundary-integral numerical solver to study porous media transport. Bhargava et al. [10] applied a finite element solver to study the free and forced convection of a micropolar rheological fluid over a stretching surface with suction effects at the wall. Bég et al. [11] employed a Blottner implicit finite difference solver to study the rotating geophysical convection in a Darcy–Forchheimer porous medium. The network simulation method (NSM) is a powerful computation-based solver employing finite-difference based discretization for systems of nonlinear, coupled ordinary and partial differential equations of any order and any degree [12]. In NSM, however, only the space variables are discretized while time remains a continuous variable. This method has been successfully employed in a diverse variety of non-porous and porous thermofluid problems. Zueco [13] analysed the hydromagnetic convection past a flat plate. More recently Zueco [14] studied the radiative–convective boundary layer flow in a porous medium using the NSM. The vast majority of porous media transport models have employed the Darcian model which for isotropic, homogenous materials, utilizes a single permeability for simulating the global effects of the porous medium on the flow. Effectively in the context of viscous hydrodynamic modelling, for example using boundary-layer theory, the momentum conservation equation (unidirectional Navier–Stokes equation) is supplemented by an additional body force, the Darcian bulk linear drag. Numerous studies in the context of transport modelling in soil mechanics, petroleum displacement in reservoirs, geothermics, geohydrology and filtration physics have employed such an approach. For example, Singh et al. [15] studied the free convection flow and heat transfer in a Darcian porous geomaterial using perturbation methods; this study also incorporated permeability variation via a transverse periodic function. Thomas and Li [16] analyzed numerically the unsteady coupled heat and mass transfer in unsaturated soil with a Darcy model. More recently, Chen and Ledesma [17] reported numerical solutions for heat and fluid transport in unsaturated repository clay barriers with a Darcy formulation. Bég et al. [18] used an alternating direction implicit solver to analyze the reactive, decaying groundwater transport in a Darcian aquifer model. The Darcy model assumes that the pressure drop across the geomaterial is proportional to the bulk drag force. At higher velocities, however, *inertial effects* become important and the regime is no longer *viscous dominated*. The most popular approach for simulating high-velocity transport in porous media, which may occur for example under strong buoyancy forces, through highly porous materials, etc., is the Darcy–Forchheimer drag force model. This adds a second-order (quadratic) drag force to the momentum transport equation. This term is related to the geometrical features of the porous medium and is independent of viscosity, as has been shown rigorously by Dybbs and Edwards [19]. The philosophy underlying Darcy–Forchheimer formulations is that at low velocity flows the Darcy term will dominate and at higher velocities the Forchheimer term will take precedence since the square of a large velocity will override the single value of the velocity. As such it has been highlighted by, for example, Bég [20] that both terms are infact intrinsically linked. The Forchheimer extension to the Darcian model has been shown to dominate in the strong inertial flow regime, as described by Skjetne and Auriault [21]. In this regime (obviously beyond the Darcy regime) the pore Reynolds number is of value equal to unity (or greater). In fact, in some cases, researchers have delineated Darcy and Darcy–Forchheimer flows based on a Reynolds number as high as 10, although inertial effects may begin to influence the flow development after a Reynolds number of unity is achieved. Numerous studies have been communicated in heat, mass (dispersion) and fluid transport using the Darcy–Forchheimer model. Mei and Auriault [22] utilized an expansion technique to study weakly quadratic drag effects in seepage. Firdaouss et al. [23] presented a comprehensive semi-empirical analysis of Darcy–Forchheimer flow models in the context of seepage and packed bed reactors. Other purely hydrodynamic Darcy–Forchheimer models have been discussed by Rasoloarijaona and Auriault [24] and Lage [25], the latter also considering the development of extremely high speed flows including turbulence effects. In the context of coupled heat and mass transfer studies, Takhar et al. [26] studied the double-diffusive heat and species transport in porous media using the Darcy–Forchheimer model. Takhar and Bég [27] used the Keller–Box implicit difference method to analyze the viscosity and thermal conductivity effects in boundary layer thermal convection in non-Darcian porous media. Bég et al. [28] studied the biomagnetic

heat-conducting blood flow through non-Darcian porous tissue using finite difference and finite element codes. Very recently Bég et al. [29] studied using NSM the unsteady hydrodynamic Couette flow through a rotating porous medium channel using a Forchheimer-extended Darcian model. In the present study we consider the heat and mass diffusion through a Darcy–Forchheimer porous regime adjacent to an impulsively started surface with thermal radiation effects. Such a model is useful in analyzing sudden species releases from, for example, a clay barrier near radioactive waste material in soils. Generally, in purely radiative heat transfer analysis, the integro-differential equation has to be solved under pertinent boundary conditions. To simplify this challenge, engineers have generally employed algebraic radiative flux models, which include the Schuster–Schwartzchild two-flux model, the Milne–Eddington approximation, the Chandrasekhar discrete ordinates method, Rosseland diffusion flux model and others. An excellent discussion of such models is available in the treatise by Siegel and Howell [30]. In the present study we shall employ the Rosseland model which has been shown to be accurate at simulating optically thick fluids which are gray, absorbing and emitting but not scattering. The energy conservation equation (heat diffusion) is therefore supplemented by an extra thermal radiation flux term. Several authors have studied radiative effects on heat transport in non-porous and porous media using the Rosseland model. Hossain and Takhar [31,32] studied, respectively, the radiative–convective flow past a vertical surface and vertical cylinder with the Rosseland flux formulation. Chamkha et al. [33] investigated the radiative-convective viscoelastic flow past a wedge geometry embedded in a Darcy–Forchheimer porous medium using an implicit difference solver, with applications in magmatic geological flows. These studies did not, however, consider time-dependent effects. In geological radioactive waste migration, as discussed by Domenico and Schwartz [34] and Bear [35], the influence of time on dispersion phenomena is of great importance. Flow patterns may take years, if not decades to develop. Recently Bég et al. [36] have therefore studied the radiative-convective heat and species diffusion in unsteady flow through a Darcian porous medium, using the Rosseland model. The present model studies the effect of time more rigorously on the near-field dynamics and also the influence of quadratic drag on flow, heat and species diffusion fields in 2D buoyancy-driven heat and species diffusion near a vertical barrier (e.g., clay wall) in a geological porous regime. The interaction of porous media hydrodynamic effects and radiative heat transfer and buoyancy are also addressed in detail. NSM incorporating the transient solver Pspice is used. Such a study has to the authors' knowledge not appeared thus far in the literature despite immediate applications to computational waste dispersion in geosystems. In future studies, a decay model for the species will also be incorporated.

2 Transport model

Consider the laminar time-dependent viscous buoyancy-driven heat and species transfer in an incompressible, absorbing, emitting and non-scattering, gray Newtonian fluid past an impulsively started vertical semi-infinite vertical barrier surface adjacent to an isotropic, homogenous non-Darcian porous medium. The medium is assumed to be non-deformable and thermal stratification and tortuosity effects are ignored. The X^* direction is located parallel to the plate surface and the Y^* direction normal to it. The barrier and fluid are taken to be at the same temperature. The physical regime is shown in Fig. 1. The concentration of species diffusing in the binary mixture (groundwater and species) is significantly less than the concentration of chemical waste (species) otherwise present. At time $t^* = 0$, the vertical barrier is heated instantaneously, i.e. impulsively (coinciding with a sudden species release) and commences impulsive motion in the positive (upward) X^* direction, with constant velocity, $u_o{}^*$, and the barrier temperature and concentration levels are instantaneously elevated. These new values are sustained for all time $t^* > 0$. Thermal radiation is assumed to be present in the form of a unidirectional flux in the Y^* direction, i.e. q_r (transverse to the vertical surface), owing to the presence of radioactive waste on the opposite side of the barrier. The Rosseland diffusion flux model is implemented to simulate radiative heat transfer and takes the form, following Siegel and Howell [30] as follows:

$$q_r = -\frac{4\sigma}{3\kappa'}\frac{\partial T^{*4}}{\partial Y^*}. \tag{1}$$

We are primarily concerned with the *near field* flow dynamics and therefore adopt a boundary-layer model in the vicinity of the barrier. Under the Boussinesq approximation, the boundary-layer equations for mass, momentum, heat and species (contaminant) conservation in an (X^*, Y^*) coordinate system can be shown to

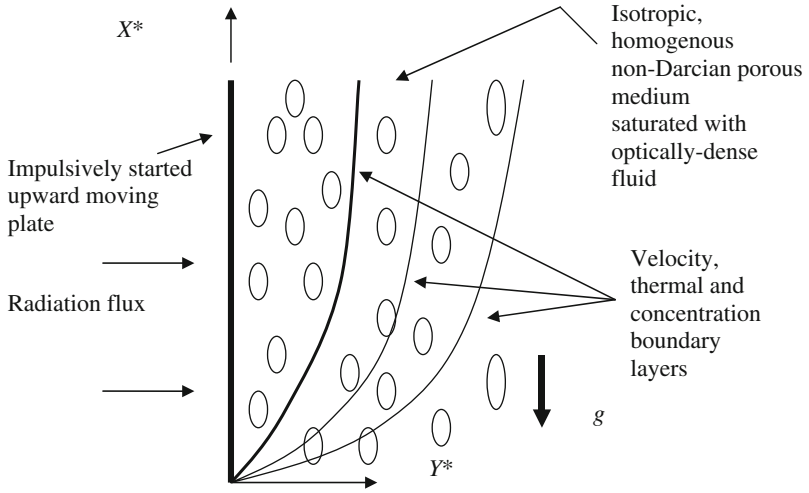

Fig. 1 Physical model and coordinate system

take the form:

$$\text{Mass conservation:} \quad \frac{\partial U^*}{\partial X^*} + \frac{\partial V^*}{\partial Y^*} = 0, \tag{2}$$

$$\text{Momentum conservation:} \quad \frac{\partial U^*}{\partial t^*} + U^*\frac{\partial U^*}{\partial X^*} + V^*\frac{\partial U^*}{\partial Y^*} = g\beta[T^* - T^*_\infty] + g\beta^*[C^* - C^*_\infty] + \nu\frac{\partial^2 U^*}{\partial Y^{*2}} - \frac{\nu}{K}U^* - \frac{b}{K}U^{*2}, \tag{3}$$

$$\text{Thermal energy conservation:} \quad \frac{\partial T^*}{\partial t^*} + U^*\frac{\partial T^*}{\partial X^*} + V^*\frac{\partial T^*}{\partial Y^*} = \alpha\frac{\partial^2 T^*}{\partial Y^{*2}} - \frac{1}{\rho C_p}\frac{\partial q_r}{\partial Y^*}, \tag{4}$$

$$\text{Species conservation:} \quad \frac{\partial C^*}{\partial t^*} + U^*\frac{\partial C^*}{\partial X^*} + V^*\frac{\partial C^*}{\partial Y^*} = D\frac{\partial^2 C^*}{\partial Y^{*2}}. \tag{5}$$

The corresponding boundary conditions in X^*–Y^* space and time (t^*) are prescribed as:

$$t^* = 0 : U^* = 0, \quad V^* = 0, \quad T^* = 0, \quad C^* = 0, \tag{6a}$$

$$t^* > 0 : U^* = U^*_o, \quad V^* = 0, \quad T^* = T^*_w, \quad C^* = C^*_\infty \quad \text{at} \quad Y^* = 0, \tag{6b}$$

$$U^* = 0, \quad T^* = T^*_\infty, \quad C^* = C^*_\infty \quad \text{at} \quad X^* = 0, \tag{6c}$$

$$U^* \to 0, \quad T^* \to T^*_\infty, \quad C^* \to C^*_\infty \quad \text{as} \quad Y^* \to \infty, \tag{6d}$$

where X^* and Y^* are coordinates, U^*, V^* are velocity components in the X^*, Y^* directions, t^* is dimensional time, σ is the Stefan–Boltzmann constant, g is gravitational acceleration, k' is the mean absorption coefficient for thermal radiation, β is coefficient of thermal expansion, β^* is mass transfer coefficient of expansion, ν is the kinematic viscosity of the gray fluid, T^* is temperature, C^* is species concentration, K is the permeability (hydraulic conductivity of the porous medium with dimension m^2), b is the Forchheimer geometrical inertial parameter for the porous medium, α is the thermal diffusivity, D is the species diffusivity, $()_w$ denotes conditions at the wall (vertical surface) and $()_\infty$ designates conditions in the free stream (outside the boundary layers). In the momentum equation (3) the first two terms on the right-hand side represent the thermal buoyancy body force and the species buoyancy body force, respectively. The penultimate term is the Darcian linear drag and the final term is the Forchheimer quadratic drag force. Following Raptis [37], we can express the quartic temperature function in Eq. (1) as a linear function of temperature. We expand therefore T^{*4} in a Taylor series about $T^*{}_\infty$, which after neglecting of higher order terms reduces to

$$T^{*4} \quad \sim 4T^{*\,3}_\infty T^* - 3T^{*\,4}_\infty. \tag{7}$$

Substitution of this expression into Eq. (1) and then the heat conservation equation (4), eventually leads to the following form of the energy equation:

$$\frac{\partial T^*}{\partial t^*} + U^* \frac{\partial T^*}{\partial X^*} + V^* \frac{\partial T^*}{\partial Y^*} = \alpha \frac{\partial^2 T^*}{\partial Y^{*2}} + \frac{16\sigma T_\infty^{*3}}{3\kappa' \rho C_p} \frac{\partial^2 T^*}{\partial Y^{*2}}. \tag{8}$$

An analytical solution of the nonlinear coupled parabolic partial differential equation system defined by Eqs. (2), (3), (5) and (8) with boundary conditions (6a) to (6d) is intractable. We therefore seek a numerical solution. Prior to solving the equations computationally using NSM, we non-dimensionalize the model. This approach allows the solutions to apply to any geometric or time scale via the use of dimensionless thermophysical and hydromechanical numbers. Proceeding with the analysis, we introduce the following quantities:

$$X = \frac{X^* U_o^*}{\nu}, Y = \frac{Y^* U_o^*}{\nu}, U = \frac{U^*}{U_o^*}, V = \frac{V^*}{U_o^*}, t = \frac{t^* U_o^{*2}}{\nu}, T = \frac{T^* - T_\infty^*}{T_W^* - T_\infty^*}, C = \frac{C^* - C_\infty^*}{C_W^* - C_\infty^*},$$
$$Pr = \frac{\nu}{\alpha}, Sc = \frac{\nu}{D}, Da = \frac{K}{L^2}, Fs = \frac{b}{L}, Re = \frac{U_o^* L}{\nu}, N = \frac{\kappa' k}{4\sigma T_\infty^{*3}}, Gr = \frac{g\beta\nu(T^*{}_w - T_\infty^*)}{U_o^{*3}},$$
$$Gm = \frac{g\beta^*\nu(C_w^* - C_\infty^*)}{U_o^{*3}}, \tag{9}$$

where X and Y are dimensionless coordinates, U and V dimensionless velocities, t is dimensionless time, T is dimensionless temperature function, C is dimensionless concentration function, N is the Stark conduction–radiation heat transfer parameter (also known as the Rosseland–Boltzmann dimensionless number in thermofluid mechanics), Pr is the Prandtl number, Sc is the Schmidt number, Da is the Darcy number, Fs is the Forcheimmer inertial number, Re is the Reynolds number, Gr is the thermal Grashof number, Gm is the species Grashof number, k is the thermal conductivity and L is a characteristic length. Introducing these transformations into Eqs. (2), (3), (5) and (8) we arrive at the following dimensionless conservation equations:

$$\frac{\partial U}{\partial X} + \frac{\partial V}{\partial Y} = 0, \tag{10}$$

$$\frac{\partial U}{\partial t} + U\frac{\partial U}{\partial X} + V\frac{\partial U}{\partial Y} = GrT + GmC + \frac{\partial^2 U}{\partial Y^2} - \left[\frac{1}{Da\,Re^2}\right]U - \left[\frac{Fs}{Da\,Re}\right]U^2, \tag{11}$$

$$\frac{\partial T}{\partial t} + U\frac{\partial T}{\partial X} + V\frac{\partial T}{\partial Y} = \frac{1}{Pr}\left[1 + \frac{4}{3N}\right]\frac{\partial^2 T}{\partial Y^2}, \tag{12}$$

$$\frac{\partial C}{\partial t} + U\frac{\partial C}{\partial X} + V\frac{\partial C}{\partial Y} = \frac{1}{Sc}\frac{\partial^2 C}{\partial Y^2}. \tag{13}$$

The corresponding initial and end boundary conditions now take the form

$$t = 0 : U = 0, \quad V = 0, \quad T = 0, \quad C = 0, \tag{14a}$$
$$t > 0 : U = 1, \quad V = 0, \quad T = 1, \quad C = 1 \quad \text{at} \quad Y = 0, \tag{14b}$$
$$U = 0, \quad T = 0, \quad C = 0 \quad \text{at} \quad X = 0, \tag{14c}$$
$$U \to 0, \quad T \to 0, \quad C \to 0 \quad \text{as} \quad Y \to \infty. \tag{14d}$$

To obtain an estimate of flow dynamics at the barrier boundary, we also define several important rate functions at $Y = 0$. These are the dimensionless *wall shear stress function, i.e. local skin friction function*, the local Nusselt number (dimensionless temperature gradient) and the local Sherwood number (dimensionless species, i.e. contaminant transfer gradient). Following Prasad et al. [38], these functions are expressed as follows:

$$\tau_X = -\left[\frac{\partial U}{\partial Y}\right]_{Y=0} \tag{15}$$

$$Nu_X = -X\left[\frac{\partial T}{\partial Y}\right]_{Y=0} \tag{16}$$

$$Sh_X = -X\left[\frac{\partial C}{\partial Y}\right]_{Y=0} \tag{17}$$

where the appropriate value for the X-coordinate can be utilized.

3 Numerical solution by NSM

Numerical solutions of the governing transformed equations (10) to (13) under boundary conditions (14a) to (14d) have been obtained using the network simulation method [39]. The starting point for this method is always the discretization of the partial differential transport equations, i.e. (10) to (13). This discretization is based on the finite-difference formulation, and only a discretization of the spatial co-ordinates is necessary, while time remains as a real continuous variable, thereby transforming the partial differential equations (PDEs) into a set of ordinary differential equations (ODEs), which can then be described by an *elemental network cell*. Unlike conventional numerical methods, in NSM the independent variable reticulation is successive since we carry out first the spatial and then the temporal reticulation to solve the circuit equations. This difference in the reticulation may provide us with some advantages in the use of the NSM, at least in certain problems. No time interval needs to be established by the users to obtain the numerical solution, the time interval is set is automatically in every iteration according to the given stability and convergence requirements, and this constitutes a strong advantage. A second advantage is that with the NSM we must only transform PDEs into ODEs and the latter along with the initial and boundary conditions must be formulated in terms of circuits. The program to solve ODEs is based on the network model. In other methods, algorithms are rather more complex and require considerable programming efforts. For the transient analysis in the Network Simulation Method, a well-tested computer package, Pspice [40] is employed which uses the *numerical implicit integration formulae* (trapezoidal integration) with a second order accuracy; additionally a central-difference methodology has been used for the approximation of first and second order spatial-derivatives. As a result, second order accuracy of the spatial discretization is achieved. Based on the governing discretized boundary layer equations, an electrical network circuit is designed for each equation, where these equations are formally equivalent to the discretized equations. The finite-difference differential equations resulting from dimensionless continuity, momentum balance, energy balance and species balance equations (10–13) are:

$$(U_{i-\Delta X,j} - U_{i+\Delta X,j})/\Delta X + (V_{i,j-\Delta y} - V_{i,j})/(\Delta Y/z) = 0, \tag{18}$$

$$\begin{aligned}&\Delta Y \mathrm{d}U_{i,j}/\mathrm{d}t + U_{i,j}(U_{i+\Delta X,j} - U_{i-\Delta X,j})\Delta Y/\Delta X + V_{i,j}(U_{i,j+\Delta Y} - U_{i,j-\Delta Y})\\ &= \Delta Y Gr T_{i,j} + \Delta Y Gm C_{i,j} + (U_{i,j-\Delta Y} - U_{i,j})/(\Delta Y/2) - (U_{i,j} - U_{i,j+\Delta Y})/(\Delta Y/2)\\ &\quad - \Delta Y U_{i,j}(1/Re + Fs U_{i,j})/(Da Re),\end{aligned} \tag{19}$$

$$\begin{aligned}&\Delta Y Pr \mathrm{d}T_{i,j}/\mathrm{d}t + U_{i,j}(T_{i+\Delta X,j} - T_{i-\Delta X,j})\Delta Y/\Delta X + \mathrm{Pr}\, V_{i,j}(T_{i,j+\Delta Y} - T_{i,j-\Delta Y})\\ &= (T_{i,j-\Delta Y} - T_{i,j})[2(1 + 4/3N^{-1})]/\Delta Y - (T_{i,j} - T_{i,j+\Delta Y})[2(1 + 4/3N^{-1})]/\Delta Y,\end{aligned} \tag{20}$$

$$\begin{aligned}&\Delta Y Sc \mathrm{d}C_{i,j}/\mathrm{d}t + \Delta Y Sc U_{i,j}(C_{i+\Delta X,j} - C_{i-\Delta X,j})/\Delta X + Sc V_{i,j}(C_{i,j+\Delta Y} - C_{i,j-\Delta Y})\\ &= (C_{i,j-\Delta Y} - C_{i,j})/(\Delta Y/2) - (C_{i,j} - C_{i,j+\Delta Y})/(\Delta Y/2).\end{aligned} \tag{21}$$

The terms that contain these equations can be treated as *electrical currents*, since the electric (i.e. motion–thermal–mass) analogy and the current Kirchhoff's law is considered [39]. This analogy can be applied in such a way that the variables velocity (U, V), temperature (T) and concentration (C) are equivalent to the variable *voltage*, while the velocity flux $(\partial U/\partial X, \partial Y/\partial Y)$, heat flux $(\partial T/\partial X, \partial T/\partial Y)$ and concentration flux $(\partial C/\partial X, \partial C/\partial Y)$ are equivalent to the variable *electric current*. NSM simulates the behavior of unsteady electric circuits by means of resistors, capacitors and non-linear devices that seek to resemble thermal systems governed by unsteady linear or non-linear equations. Another noticeable advantage of the NSM is that it provides both the velocity and velocity flux fields immediately (without the need for numerical manipulation). Later, an electrical network circuit is designed to model the boundary conditions. The whole network must be converted into a suitable program that is solved by a computer code using the robust software Pspice [40] in this work. A mesh system with 20×200 nodes is proven to suggest mesh-independent results. An advantage of the NSM is that the derivatives involved in Eqs. (18) to (21) are directly evaluated, while other methods for example use a *five-point approximation formula*. The integrals (15) to (17) are evaluated using the Newton–Cotes closed integration formula. In NSM we define therefore the following currents:

(i) Momentum (hydrodynamic) balance

$$j_{U,i,j+\Delta Y} = (U_{i,j} - U_{i,j+\Delta Y})/(\Delta Y/2), \tag{22a}$$
$$j_{U,i,j-\Delta Y} = (U_{i,j-\Delta Y} - U_{i,j})/(\Delta Y/2), \tag{22b}$$
$$j_{U\theta,i,j} = \Delta Y Gr T_{i,j}, \tag{22c}$$
$$j_{UC,i,j} = \Delta Y Gm C_{i,j}, \tag{22d}$$
$$j_{UDa,i,j} = \Delta Y/DaRe^2 U_{i,j}, \tag{22e}$$
$$j_{Ux,i,j} = \Delta Y U_{i,j}(U_{i+\Delta X,j} - U_{i-\Delta X,j})/\Delta X, \tag{22f}$$
$$j_{Uy,i,j} = V_{i,j}(U_{i,j+\Delta Y} - U_{i,j-\Delta Y}), \tag{22g}$$
$$j_{U\tau,i,j} = \Delta Y \mathrm{d}U_{i,j}/\mathrm{d}t. \tag{22h}$$

$j_{U,i,j+\Delta Y}$ and $j_{U,i,j-\Delta Y}$ are the currents that leave and enter the cell for the friction term of U, $j_{U,i,j}$ the current due the buoyancy term, $j_{Ux,i,j}$ and $j_{Uy,i,j}$ are the currents due the inertia terms of U and V, respectively, while $j_{U\tau,i,j}$ is the transitory term. The currents $j_{U,i,j+\Delta Y}$ and $j_{U,i,j-\Delta Y}$ are implemented by two resistances $R_{u,i,j\pm\Delta Y}$ of value "$\Delta Y/2$", while the currents $j_{U\theta,i,j}$, $j_{UC,i,j}$, $j_{UDa,i,j}$, $j_{Ux,i,j}$ and $j_{Uy,i,j}$ are implemented by means of voltage control current generators. Thus, the two currents are modelled by the generator $G_{U\theta C,i,j}$ with the control action "$\Delta Y(GrT_{i,j} + GmC_{i,j})$", while the other currents are modelled with the generators $G_{UDa,i,j}$, $G_{U,\Delta X,i,j}$ and $G_{U,\Delta Y,i,j}$, respectively, by means of the voltages "$\Delta Y/DaRe^2U_{i,j}$", "$\Delta Y U_{i,j}(U_{i+\Delta X,j} - U_{i-\Delta X,j})/\Delta X$" and "$V_{i,j}(U_{i,j+\Delta Y} - U_{i,j-\Delta Y})$", respectively; $U_{i+\Delta X,j}$, $U_{i-\Delta X,j}$, $U_{i,j+\Delta Y}$ and $U_{i,j-\Delta Y}$ are the voltages (velocities) of the nodes "$i+\Delta X$, j", "$i-\Delta X$, j", "i, $j+\Delta Y$" and "i, $j-\Delta Y$" in the cell of the momentum equation, while $U_{i,j}$ is the velocity in the centre of this cell (i, j) and $j_{U\tau,i,j}$ is implemented by one capacitor of value $C_{u,i,j} = \Delta Y$, connected to the center of each cell. The Forchheimer term has been omitted above for brevity.

(ii) Energy (heat) equation

$$j_{T,i,j+\Delta Y} = (T_{i,j} - T_{i,j+\Delta Y})/[\Delta Y/2(N + 4/3)], \tag{23a}$$
$$j_{T,i,j-\Delta Y} = (T_{i,j-\Delta Y} - T_{i,j})/[\Delta Y/2(N + 4/3)], \tag{23b}$$
$$j_{Tx,i,j} = \Delta Y U_{i,j} PrN(\theta_{i+\Delta X,j} - \theta_{i-\Delta X,j})/\Delta X, \tag{23c}$$
$$j_{Ty,i,j} = V_{i,j} PrN(\theta_{i,j+\Delta Y} - \theta_{i,j-\Delta Y}), \tag{23d}$$
$$j_{T\tau,i,j} = \Delta Y PrN d\theta_{i,j}/dt. \tag{23e}$$

$j_{T,i,j+\Delta Y}$ and $j_{T,i,j-\Delta Y}$ are the currents that leave and enter the cell due to the transversal conduction, $j_{Tx,i,j}$ and $j_{TY,i,j}$ are the currents due the convective terms of U and V, respectively, while $j_{T\tau,i,j}$ is the transitory term. The currents $j_{T,i,j+\Delta Y}$ and $j_{T,i,j-\Delta Y}$ are implemented by means of two resistances $R_{T,i,j\pm\Delta Y}$ of value "$\Delta Y/2$", while the currents $j_{Tx,i,j}$ and $j_{Ty,i,j}$ are implemented by voltage control current generators $G_{T,\Delta X,i,j}$ and $G_{T,\Delta Y,i,j}$, respectively; these voltages are "$\Delta Y U_{i,j} PrN(T_{i+\Delta X,j} - T_{i-\Delta X,j})/\Delta X$" and "$V_{i,j} PrN(T_{i,j+\Delta Y} - T_{i,j-\Delta Y})$", respectively; being $T_{i+\Delta X,j}$, $T_{i-\Delta X,j}$, $T_{i,j+\Delta Y}$ and $T_{i,j-\Delta Y}$ the voltages (temperature) of the nodes "$i+\Delta X$, j", "$i-\Delta X$, j", "i, $j+\Delta Y$" and "i, $j-\Delta Y$" in the cell of the energy balance, while $T_{i,j}$ is the temperature in the center of the cell (i, j). $j_{T\tau,i,j}$ is implemented by means of one capacitor of value $C_{T,i,j} = \Delta Y NPr$, connected to the center of each cell.

(iii) Contaminant (concentration) equation

$$j_{C,i,j+\Delta Y} = (C_{i,j} - C_{i,j+\Delta Y})/(Sc\Delta Y/2), \tag{24a}$$
$$j_{C,i,j-\Delta Y} = (C_{i,j-\Delta Y} - C_{i,j})/(Sc\Delta Y/2), \tag{24b}$$
$$j_{Cx,i,j} = \Delta Y U_{i,j}(C_{i+\Delta X,j} - C_{i-\Delta X,j})/\Delta X, \tag{24c}$$
$$j_{Cy,i,j} = V_{i,j}(C_{i,j+\Delta Y} - C_{i,j-\Delta Y}), \tag{24d}$$
$$j_{C\tau,i,j} = \Delta Y \mathrm{d}C_{i,j}/\mathrm{d}t. \tag{24e}$$

$j_{C,i,j+\Delta Y}$ and $j_{C,i,j-\Delta Y}$ are the currents that leave and enter the cell due to the transversal conduction, $j_{Cx,i,j}$ and $j_{Cy,i,j}$ are the currents due to the convective terms of U and V, respectively, while $j_{C\tau,i,j}$ is the transitory term. The currents $j_{C,i,j+\Delta Y}$ and $j_{C,i,j-\Delta Y}$ are implemented by means of two resistances $R_{C,i,j\pm\Delta Y}$ of value "$\mathrm{Sc}\Delta Y/2$", while the currents $j_{Cx,i,j}$ and $j_{Cy,i,j}$ are implemented by means of voltage control current generators $G_{C,\Delta X,i,j}$ and $G_{C,\Delta Y,i,j}$, respectively; these voltages are "$\Delta Y U_{i,j}(C_{i+\Delta X,j} - C_{i-\Delta X,j})/\Delta X$"

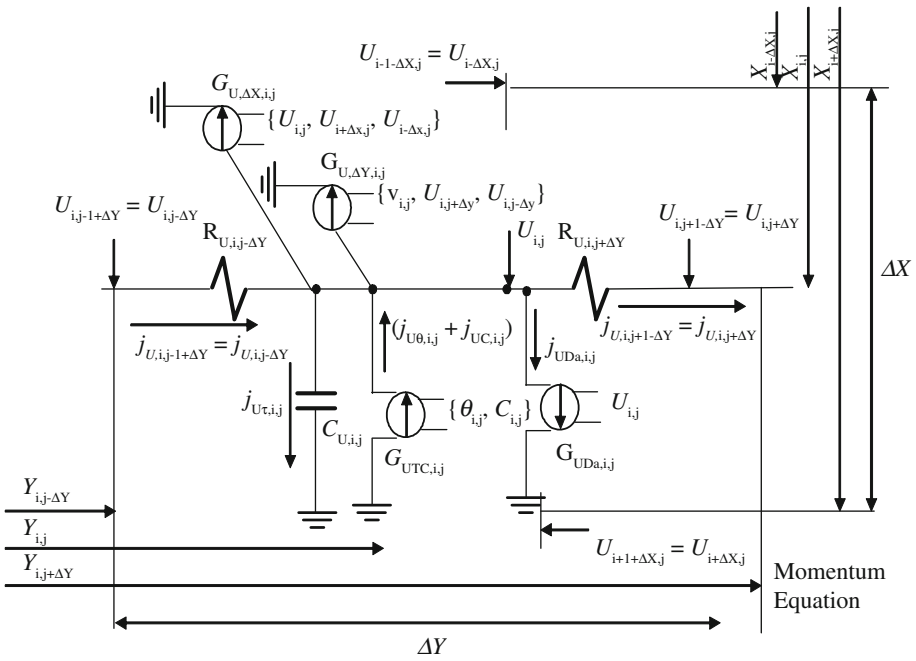

Fig. 2 Network model for momentum equation

and "$V_{i,j}(C_{i,j+\Delta Y} - C_{i,j-\Delta Y})$", respectively; being $C_{i+\Delta X,j}$, $C_{i-\Delta X,j}$, $C_{i,j+\Delta Y}$ and $C_{i,j-\Delta Y}$ the voltages (concentrations) of the nodes "$i + \Delta X$, j", "$i - \Delta X$, j", "i, $j + \Delta Y$" and "i, $j - \Delta Y$" in the cell of the mass balance, while $C_{i,j}$ is the concentration in the center of the cell (i, j). $j_{C\tau,i,j}$ is implemented by means one capacitor of value $C_{C,i,j} = \Delta Y$, connected to the center of each cell.

The finite difference equation corresponding to Eq. (18) is obtained the velocity component $V_{i,j}$. Equations (19), (20) and (21) can be written in the form of Kirchhoff's law:

$$j_{U,i,j+\Delta Y} - j_{U,i,j-\Delta Y} - j_{U\theta,i,j} - j_{UC,i,j} + j_{UDa,i,j} + j_{U2Fs,i,j} + j_{Ux,i,j} + j_{Uy,i,j} + j_{U\tau,i,j} = 0, \quad (25a)$$

$$j_{T,i,j+\Delta Y} - j_{T,i,j-\Delta Y} + j_{Tx,i,j} + j_{Ty,i,j} + j_{T\tau,i,j} = 0, \quad (25b)$$

$$j_{C,i,j+\Delta Y} - j_{C,i,j-\Delta Y} + j_{Cx,i,j} + j_{Cy,i,j} + j_{C\tau,i,j} = 0. \quad (25c)$$

Figures 2, 3 and 4 show the *network models* corresponding to Eqs. (25a), (25b) and (25c). Finally, to implement the velocity, temperature and concentration boundary conditions (at $X = 0$ and as $Y \to \infty$) *ground elements* are employed, while a constant voltage of value unity is employed at $Y = 0$. Regarding the initial condition, the voltages $U = \theta = C = 0$ for $t \leq 0$ are applied to the three capacitors $C_{U,i,j}$, $C_{T,i,j}$ and $C_{C,i,j}$.

4 Results and discussion

To test the accuracy of the NSM simulations we have compared the transient velocity profiles versus Y at $X = 1.0$ and the steady-state local skin friction distributions versus the axial coordinate X for various combinations of Gr, Gm, Sc and N with the Crank–Nicolson central difference computations of Prasad et al. [38]. The comparisons are shown in Figs. 5 and 6 and found to be in excellent agreement. Prasad et al. [38] used the reduced momentum equation

$$\frac{\partial U}{\partial t} + U\frac{\partial U}{\partial X} + V\frac{\partial U}{\partial Y} = GrT + GmC + \frac{\partial^2 U}{\partial Y^2}. \quad (26)$$

In this scenario the Darcian drag vanishes implying that the porous matrix permeability becomes infinite so that the regime is purely fluid; Forchheimer drag also vanishes. The comparisons shown in Figs. 5 and 6

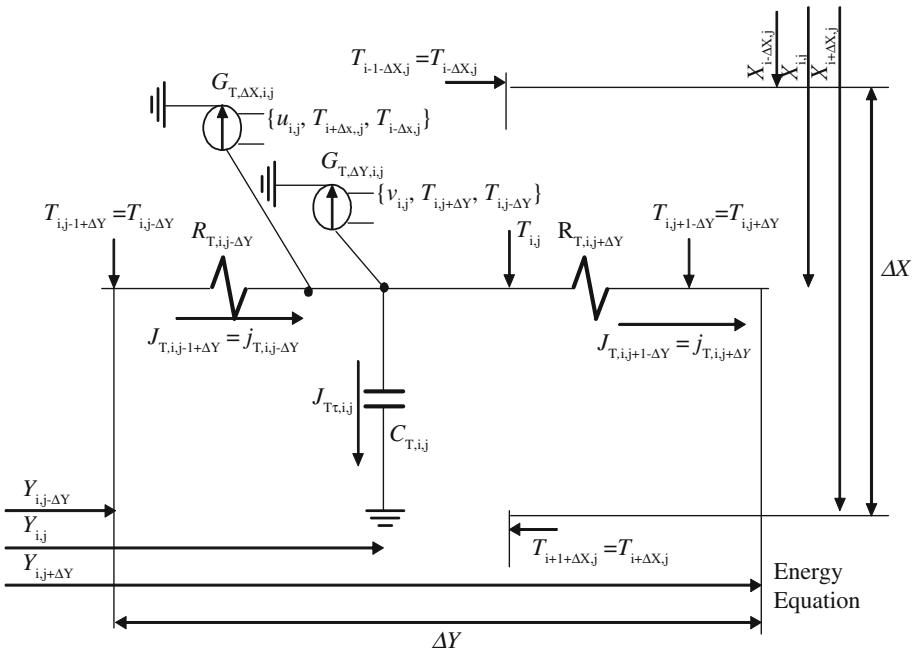

Fig. 3 Network model for energy equation

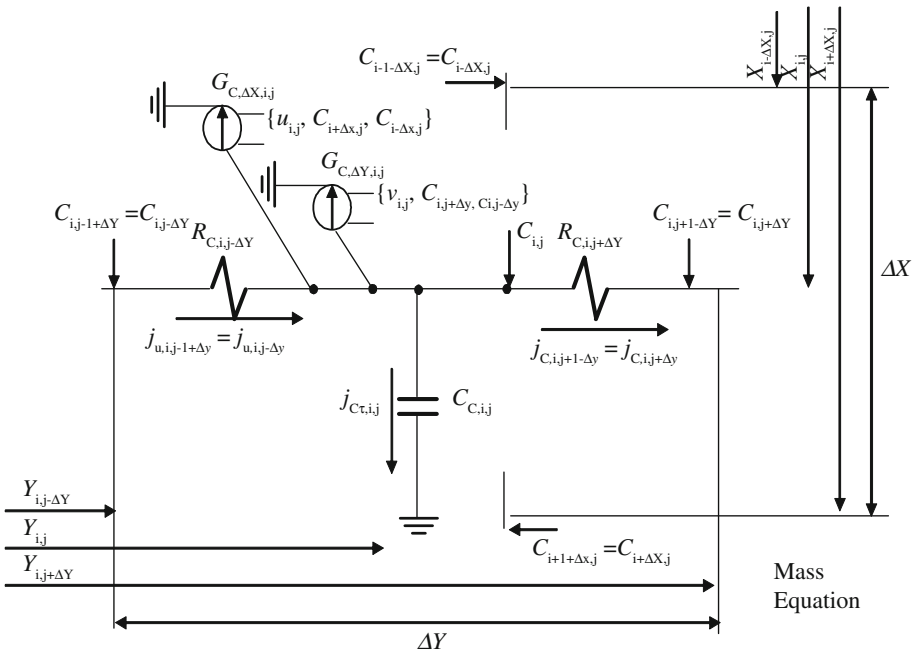

Fig. 4 Network model for contaminant (species concentration) equation

and found to be in excellent agreement. In Fig. 6 *steady-state* refers to a significant elapsed time after which all impulsive effects have been smoothed out.

Figure 7 shows the transient distribution of dimensionless temperature with the X coordinate through the porous medium, at $t = 1$ and $Y = 1.25$, for various thermal Grashof numbers. This parameter defines the relative effects of *thermal buoyancy* (due to density differences) and *viscous hydrodynamic force* in the flow. A rise in Gr clearly generates a decrease in temperature, i.e. buoyancy depresses the value of temperature along the barrier wall. We observe that values increase dramatically owing to the impulsive thermal effects at

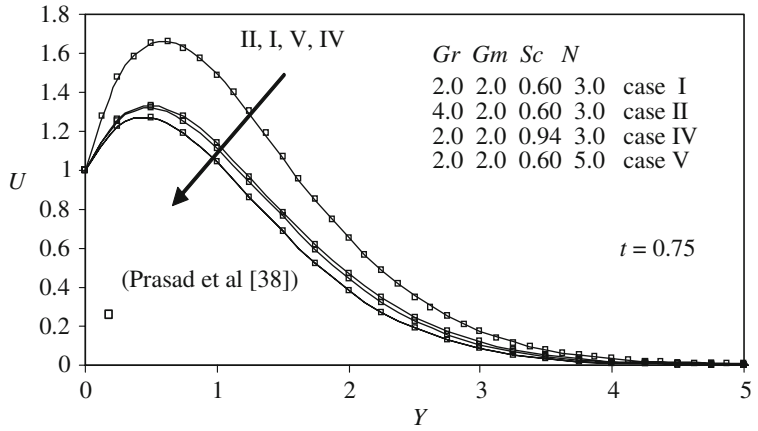

Fig. 5 Transient velocity profiles at $X = 1.0$ for various values of Gr, Gm, Sc and N

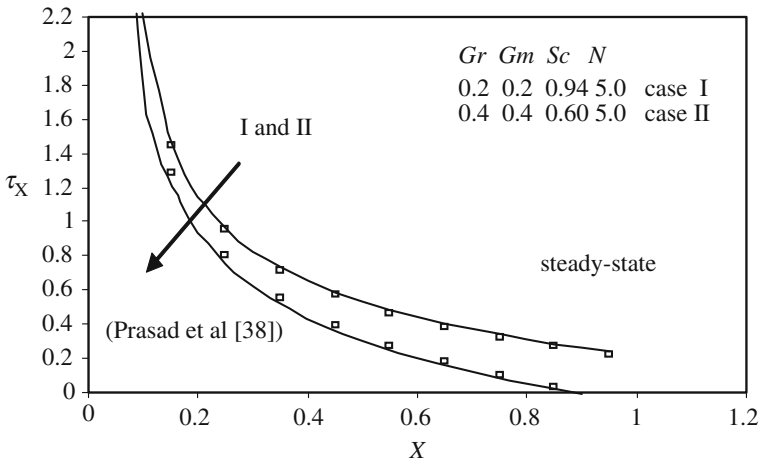

Fig. 6 Steady state local skin friction profiles versus X for various values of Gr, Gm, Sc and N

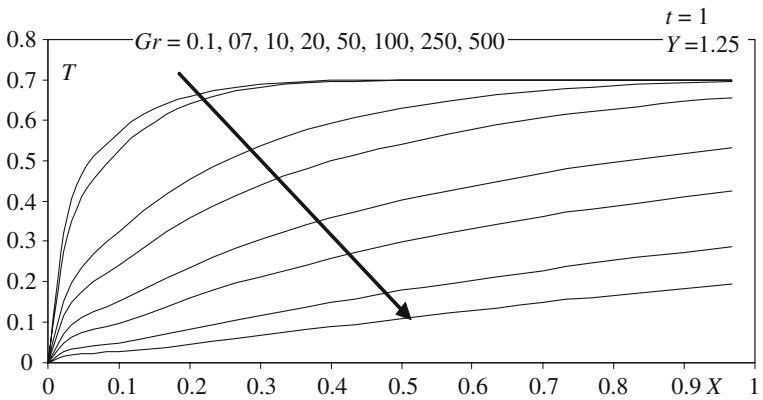

Fig. 7 Transient temperature distribution with X at $Y = 1.25$ and $t = 1$ for various values of Gr

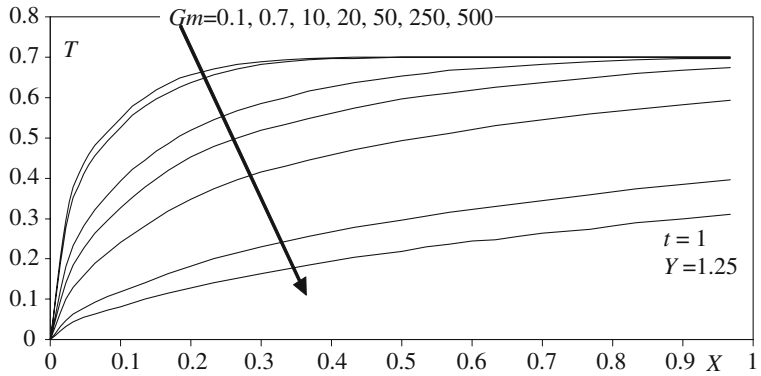

Fig. 8 Transient temperature distribution with X at $Y = 1.25$ and $t = 1$ for various values of Gm

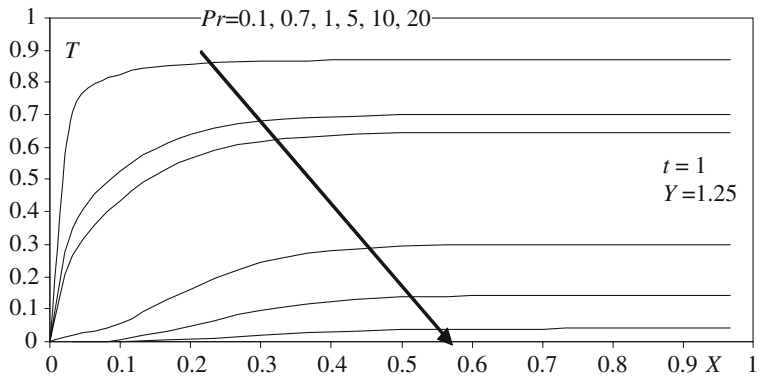

Fig. 9 Transient temperature distribution with X at $Y = 1.25$ and $t = 1$ for various values of Pr

$t = 0$ from the lowest point of the barrier, i.e. $X = 0.0$ and then gradually smoothen out. Peak temperatures correspond to the lowest Gr value, namely $Gr = 0.1$. A similar trend is observed for the effects of *species Grashof number*, Gm, on T versus X profiles (Fig. 8), again at $t = 1$ and $Y = 1.25$. Gm defines the ratio of the species buoyancy force to the viscous hydrodynamic force. For high concentration differences, Gm will therefore assume a higher value and we observe that for $Gm = 500$, the temperatures are minimized along the X direction in the soil medium. To study the effects of the relative contribution of momentum diffusion and thermal diffusion in the thermal contaminant transport, we study next the influence of Prandtl number, Pr, on temperature distribution with X coordinate, as shown in Fig. 9. Pr represents the ratio of momentum and thermal diffusivities. Low Pr fluids correspond to low density gases; higher Pr values are associated with denser fluids, for example $Pr = 10$ represents contaminated water, $Pr = 20$ more densely polluted water. With greater contaminant presence in the regime, diffusing from the barrier, we observe that Pr increases and this serves to strongly reduce the temperature values. Pr also defines the relative effectiveness of momentum diffusion in the velocity boundary layer to heat diffusion in the thermal boundary layer. These phenomena are of the same order of magnitude for the special case when $Pr = 1$. For values less than unity (e.g., 0.1, 0.7 as considered in Fig. 6), the heat will diffuse faster than the momentum and this causes higher temperature values for lower Pr. For values of Pr higher than unity, for example $Pr = 5, 10, 20$, the momentum will diffuse faster than the heat through the porous geomaterial leading to an increase in velocity and decrease in temperatures.

Figures 10, 11, 12 and 13 illustrate the effects of Gr, Gm, Pr and Sc, respectively, on the *transient velocity distribution* parallel to the barrier wall, i.e. the U velocity component. Again we have selected isochrones corresponding to $t = 1$ at the location $Y = 1.25$. The erratic behaviour for low t corresponds to impulsive effects due to an instantaneous rise in temperature when hot contaminant is released in the geomaterial. In Fig. 10, we see that after $t = 0.1$, profiles climb steadily and become increasingly divergent as we approach the upper regions of the barrier, i.e. the maximum separation of U values corresponds to $X = 0.5$. A decrease in Gr causes a significant decrease in transient velocity, U. Therefore, with a decrease in buoyancy force due to temperature differences, the flow is decelerated in the geomaterial. The peak transient velocity, U, corresponds

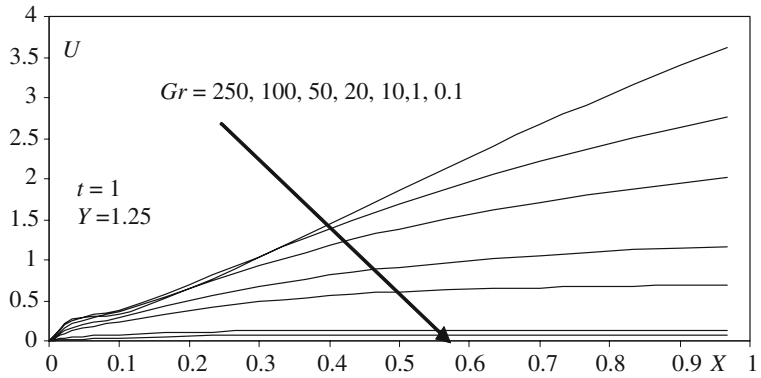

Fig. 10 Transient velocity distribution with X at $Y = 1.25$ and $t = 1$ for various values of Gr

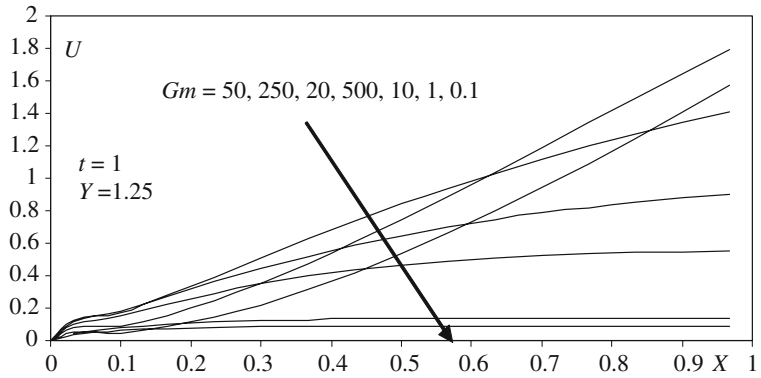

Fig. 11 Transient velocity distribution with X at $Y = 1.25$ and $t = 1$ for various values of Gm

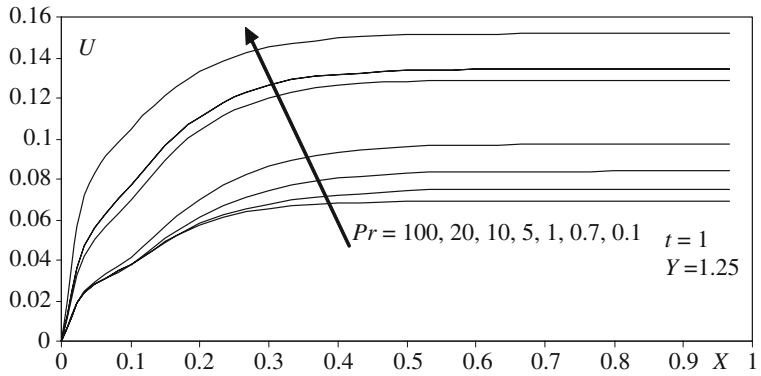

Fig. 12 Transient velocity distribution with X at $Y = 1.25$ and $t = 1$ for various values of Pr

to a maximum Gr of 250, for which the thermal buoyancy force is approximately 250 times the magnitude of the viscous hydrodynamic force in the flow. The effect of Gm (shown in Fig. 11) on the transient velocity does not follow the same trend as for the thermal buoyancy parameter Gr. For $Gm = 50$ the maximum U values are observed but only along the wall as far as $X = 0.6$. For $Gm = 250$, although values are initially lower than for $Gm = 50$, for $X > 0.6$ these values exceed those for $Gm = 50$. For $Gm = 500$, the values are consistently smaller than for either $Gm = 50$ or 250. With a further decrease in Gm, from 10, to 1, to 0.1, we note that the velocity U stays significantly below its value for $Gm = 500$. Overall it would appear therefore that a critical species Grashof number is associated with acceleration of the flow, above which (except for very high Gm values) velocities increase towards the upper regime of the wall (barrier) and below which they decrease significantly. For very low Gm values, e.g. 0.1, the viscous hydrodynamic force is ten times the value of the species buoyancy force, causing a substantial deceleration in the flow. Figure 12 illustrates the effect of Pr on

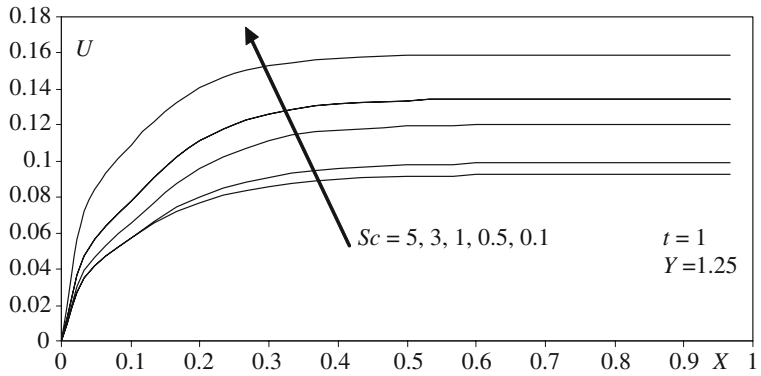

Fig. 13 Transient velocity distribution with X at $Y = 1.25$ and $t = 1$ for various values of Sc

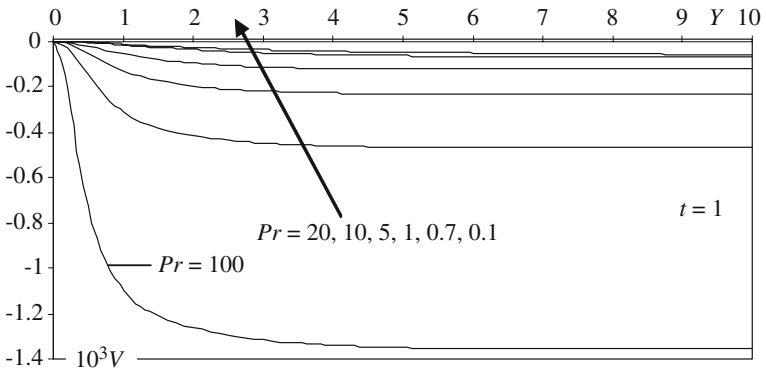

Fig. 14 Transient velocity distribution with Y at $X = 1.0$ and $t = 1$ for various values of Pr

transient velocity profiles. Increasing Pr is seen to increase the U value; a rise in Pr (above unity) implies that the momentum diffuses faster than the heat in the porous regime. As a result, clearly the velocity will increase in the regime. $Pr = 100$ corresponds to significantly viscous suspensions such as water containing dense toxic wastes and as such the ability to transport momentum is large. The velocity boundary layer is therefore thicker and velocities are greater. The no-slip condition requires that the flow velocity at the surface of a solid object (i.e. barrier) is zero and that the fluid temperature is equal to the surface temperature. The thermal boundary layer thickness is similarly the distance from the body at which the temperature is 99% of the temperature found from an inviscid solution. The *ratio of the two thicknesses* is governed by the Prandtl number. If the Prandtl number is 1, the two boundary layers are of the same thickness. If the Prandtl number is greater than 1, the thermal boundary layer is thinner than the velocity boundary layer. Generally, higher Pr fluids will have relatively low thermal conductivities which will reduce the conduction heat transfer and increase temperature variations. Convective heat transfer will be increased. If the Prandtl number is less than 1 (i.e. 0.1, 0.7 in Fig. 12), the thermal boundary layer is thicker than the velocity boundary layer, and convection heat transfer is reduced in the geomaterial. Figure 10 shows the effect of the Schmidt number on the transient velocity distribution with the X coordinate. A rise in Sc is seen to significantly depress the velocity values. Also we note that since Pr does not equal Sc generally in our computations (they are 0.7 and 0.5, respectively), the thermal and species diffusion regions will be of different extents. Only when $Pr = Sc$ will these regions be of approximately the same extent. Sc symbolizes the relative effectiveness of momentum diffusion in the velocity boundary layer to species diffusion in the concentration boundary layer. Larger Sc fluids will possess lower mass diffusion characteristics. The Schmidt number is the ratio of the shear component for diffusivity *viscosity/density* to the diffusivity for mass transfer D. It physically relates the relative thickness of the hydrodynamic boundary layer and mass-transfer (concentration) boundary layer.

Figures 14–20 show the effects of Pr, Fs, N, Da, Gr, Gm and Sc, respectively, on the *transient velocity distribution* perpendicular to the barrier wall, i.e. the velocity component V with distance Y normal to the barrier wall. As with the U distributions, we have selected isochrones corresponding to $t = 1$. It is apparent that in all cases the velocity V is negative, indicating significant backflow in the regime as we move

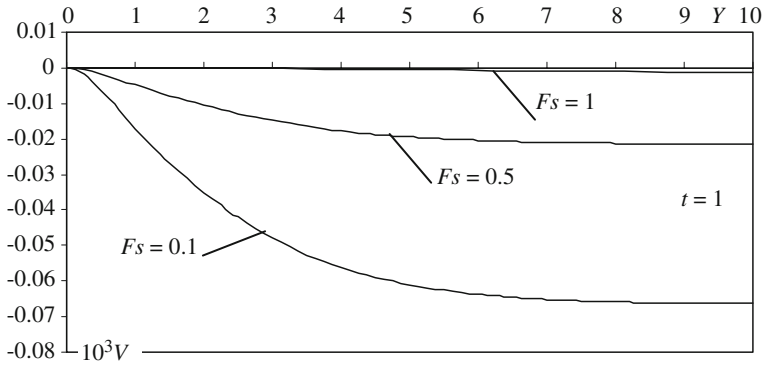

Fig. 15 Transient velocity distribution with Y at $X = 1.0$ and $t = 1$ for various values of Fs

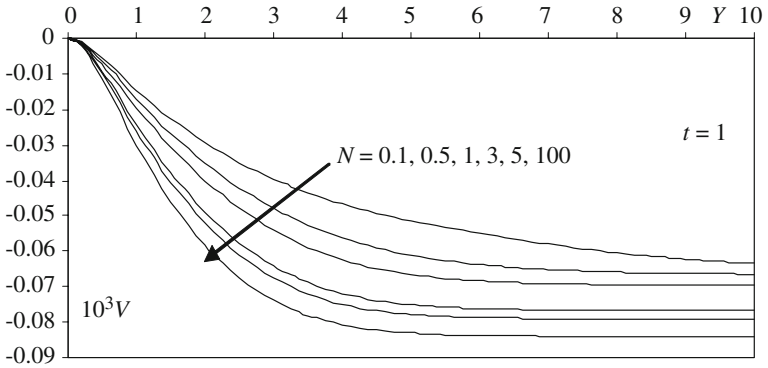

Fig. 16 Transient velocity distribution with Y at $X = 1.0$ and $t = 1$ for various values of N

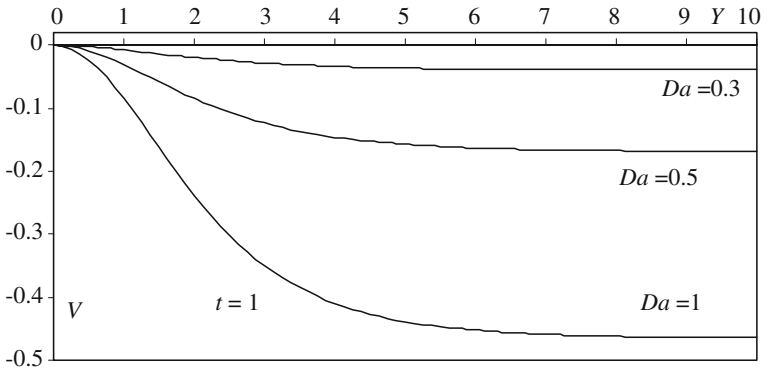

Fig. 17 Transient velocity distribution with Y at $X = 1.0$ and $t = 1$ for various values of Da

from the barrier well into the geomaterial boundary layer regime. A rise in Pr from 0.1, 0.7, 1, 5, 10, 20 through to 100 causes a significant rise in the magnitude of V throughout the regime. An increase in Fs (Fig. 15) causes a rise in the inertial drag exerted on the fluid, thermal and contaminant fields and therefore a deceleration in the flow. V values are therefore substantially reduced in magnitude as Fs increases from 0.1, through 0.5 to 1.0. The influence of thermal radiation, simulated via the Stark number, N, on V versus Y profiles is shown in Fig. 16. N defines the relative contribution of conduction heat transfer to thermal radiation transfer. Large N values imply small radiation contribution. In the limit as $N \to \infty$, thermal radiation flux vanishes. In the opposite limit as $N \to 0$, thermal radiation totally dominates thermal conduction, i.e. the latter vanishes. Hence with smaller N values, *thermal radiation* is stronger than *thermal conduction* (the contribution is only equal for both modes of heat transfer when $N = 1$), and such cases will correspond to significant concentration and *intensity* of radioactive material releases from the barrier. The transient velocity, V, is seen to *decrease* in magnitude with a decrease in N, i.e. an increase in thermal

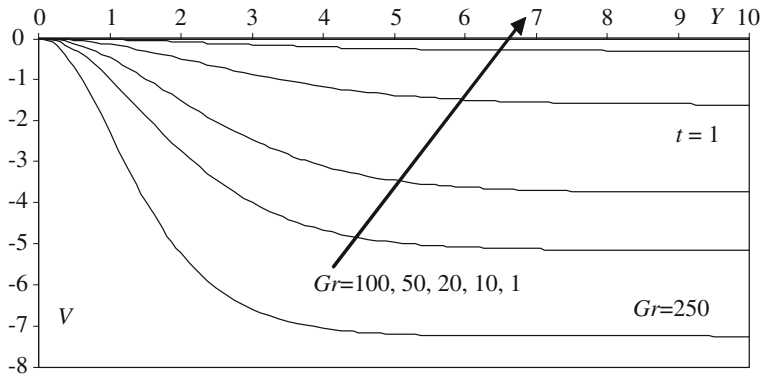

Fig. 18 Transient velocity distribution with Y at $X = 1.0$ and $t = 1$ for various values of Gr

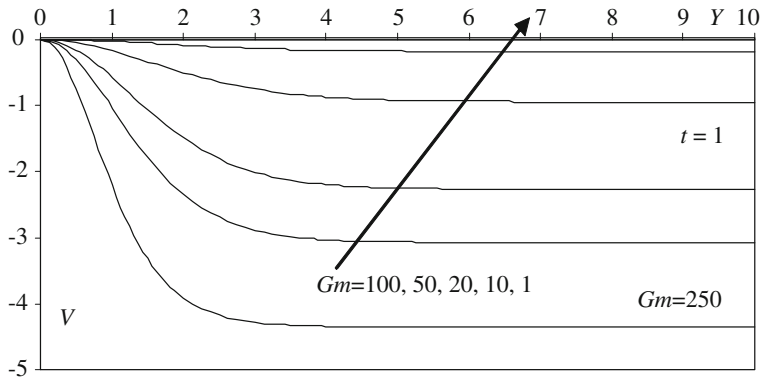

Fig. 19 Transient velocity distribution with Y at $X = 1.0$ and $t = 1$ for various values of Gm

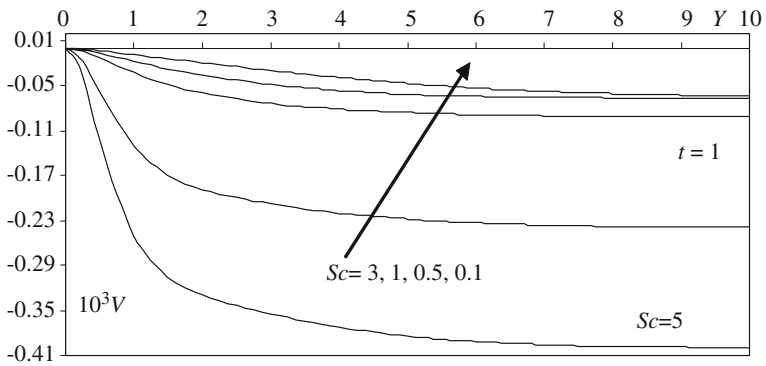

Fig. 20 Transient velocity distribution with Y at $X = 1.0$ and $t = 1$ for various values of Sc

radiation contribution. Thermal radiation supplements the fluid thermal conductivity via the energy equation and serves to *increase* temperatures, simultaneously reducing momentum transfer, i.e. decelerating the flow normal to the barrier and lowering V values in magnitude. Figure 17 shows the effect of the bulk porous medium drag parameter, Da, on V versus Y profiles. A rise in Da corresponds physically to an increase in permeability of the geomaterial. The Darcian drag force is inversely proportional to Da, i.e. with increasing Da, the porous medium impedance is progressively reduced so that the flow is accelerated, i.e. magnitudes of Y-direction transient velocity are increased. $Da = 1$ corresponds to a highly porous medium, i.e. loosely packed geomaterials. A similar response is observed with an increase in Gr and Gm parameters, i.e. the V values (Figs. 18 and 19, respectively) strongly increase in magnitude as Gr increases from 11 through 10, 20, 50 to 100 and as Gm increases through the same range. As expected a rise in Sc (Fig. 20) causes an increase in transient velocity V throughout the porous medium normal to the barrier. As discussed earlier, increasing Sc

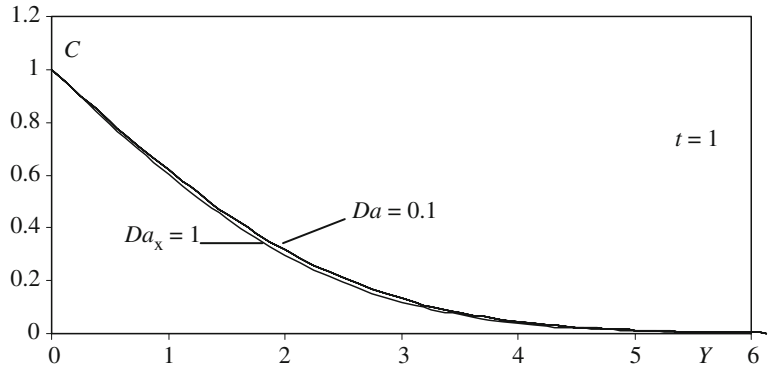

Fig. 21 Transient concentration distribution with Y at $X = 1.0$ and $t = 1$ for various values of Da

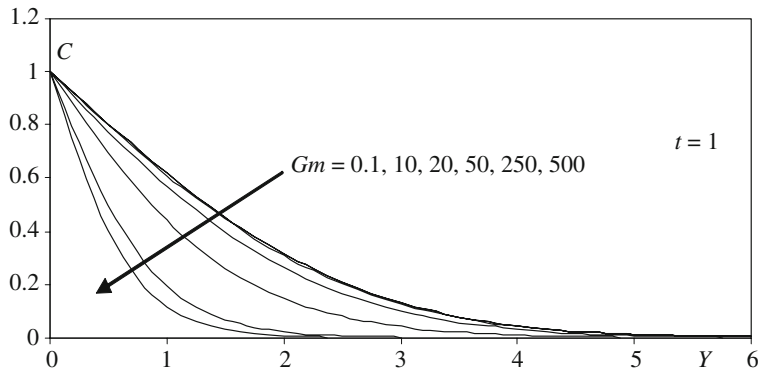

Fig. 22 Transient concentration distribution with Y at $X = 1.0$ and $t = 1$ for various values of Gm

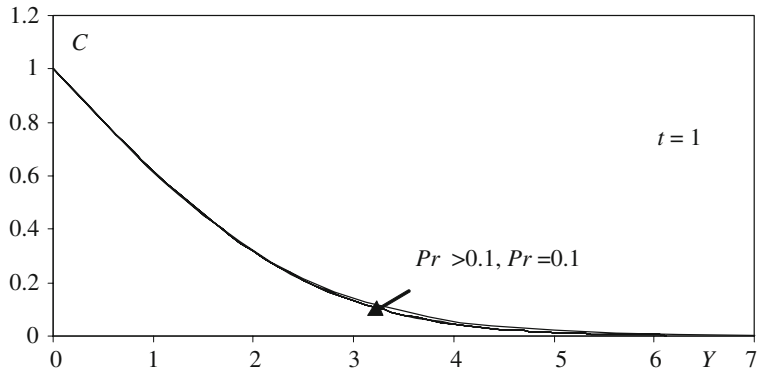

Fig. 23 Transient concentration distribution with Y at $X = 1.0$ and $t = 1$ for various values of Pr

implies an increase in momentum diffusivity compared with species diffusivity, so that the velocity boundary layer will be thinner than the concentration (contaminant) boundary layer.

Figures 21–25 show the distribution of contaminant concentration with Y direction for various Da, Gm, Pr and Sc values. Converse to the velocity response, we observe that the concentration function C in fact decreases slightly with an increase in Da (Fig. 21), i.e. *mass diffusion is decreased for greater permeability regimes*, with better transport being observed in less porous materials. An increase in Gm (Fig. 22) also substantially reduces the C profile values with Y so that increasing thermal buoyancy body force has an inhibiting effect on the value of contaminant concentration throughout the boundary layer regime normal to the barrier. As we have discussed earlier, the Gm parameter approximates the ratio of species-induced buoyancy force to viscous hydrodynamic force, which in contaminant geohydrodynamics is caused by the negative influence of buoyancy due to concentration difference on mass diffusion phenomena. Similar trends are discussed in [27]. The profiles

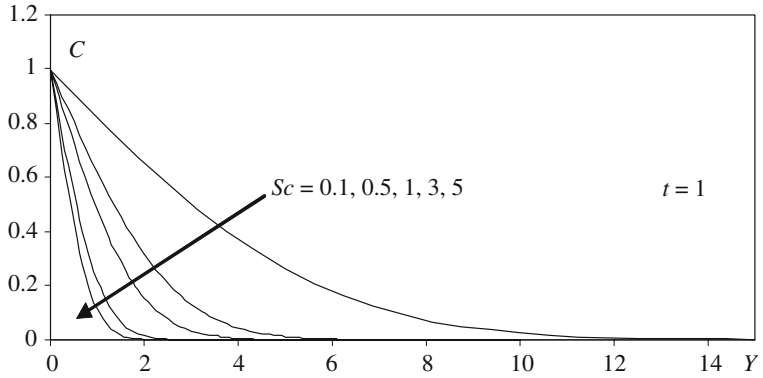

Fig. 24 Transient concentration distribution with Y at $X = 1.0$ and $t = 1$ for various values of Sc

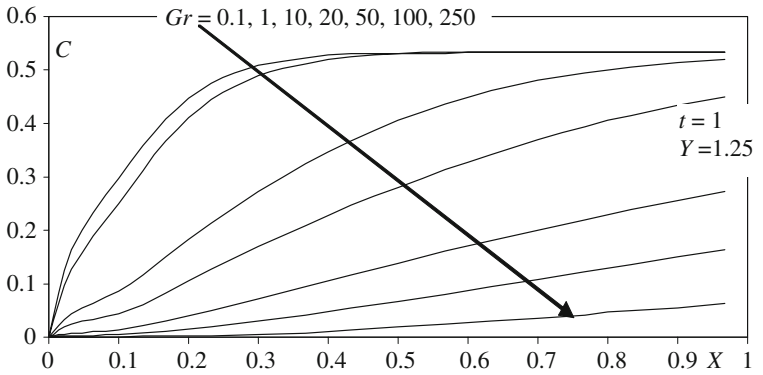

Fig. 25 Transient concentration distribution with X at $Y = 1.25$ and $t = 1$ for various values of Gr

in Fig. 22, we note, all decay monotonically from a maximum C value at $Y = 0$ (corresponding to a release at the barrier) to zero in the free stream (outside the boundary layer). Maximum differences are observed between $1 < Y < 3$, with less dramatic changes in concentration function further from the wall. Again, our computations are confined to the near-field regime of the barrier and early in the duration of a pollutant release ($t = 1$). Very little effect on mass transfer, i.e. C values, is induced by a change in Pr (Fig. 23)—a slight decrease is caused by reducing Pr values around $Y \sim 3.5$. Any changes in thermal diffusivity will be experienced in the mass diffusion equation (13) *indirectly* via the species buoyancy effect term in the momentum equation which is affected by the thermal buoyancy term in the same equation (11). Prandtl number effects on the concentration distribution will therefore be minor. Conversely we observe in Fig. 24, that a change in Sc has a significant effect on concentration distribution with the Y coordinate; a rise in Sc from 0.1 through 0.5, 1, 3, and 5 causes a considerable decrease in C values. As we have mentioned earlier, Sc embodies the relative effectiveness of momentum diffusion to species (contaminant) diffusion. When $Sc = 1$, both diffusive mechanisms will be of the same order. For $Sc > 1$, momentum will dominate, i.e. less diffusion will occur of the contaminant. For $Sc < 1$, species diffusivity will be dominant and greater mass diffusion will occur, explaining the higher values of C for Sc values of 0.1 and 0.5.

Figures 25–30 show the distribution of contaminant concentration with X (along the barrier wall) at $t = 1$ and $Y = 1.25$, for various values of Gr, Fs, Da, Gm, Pr and Sc. Increasing Gr values (Fig. 25) are seen to considerably reduce concentration function values (C) throughout the extent of the barrier length ($0 < X < 1$). An increase in the Forchheimer parameter (Fs), shown in Fig. 26, is seen to boost the concentration distribution in particular in the regime $0 < X < 0.4$, i.e. as Forchheimer drag increases, and the flow field is decelerated, contaminant is found to increase in concentration along the wall. The slower flow in the geomaterial, therefore, does not have time to distribute contaminant along the wall, which accounts for higher values of C at the lower vicinity with increasing Fs values. For $X > 0.4$, all profiles converge, i.e. Fs has negligible effect on C values further up the barrier wall. Figure 27 shows that a rise in the Darcy number, Da, corresponding to increasing permeability of the regime, while accelerating the flow (as shown earlier) serves to strongly decrease the concentration magnitudes in the geomaterial. Variations are particularly large in the region $0 < X < 0.6$. A less

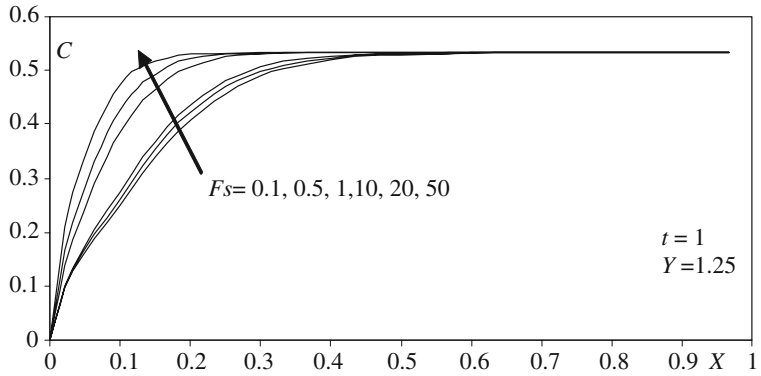

Fig. 26 Transient concentration distribution with X at $Y = 1.25$ and $t = 1$ for various values of Fs

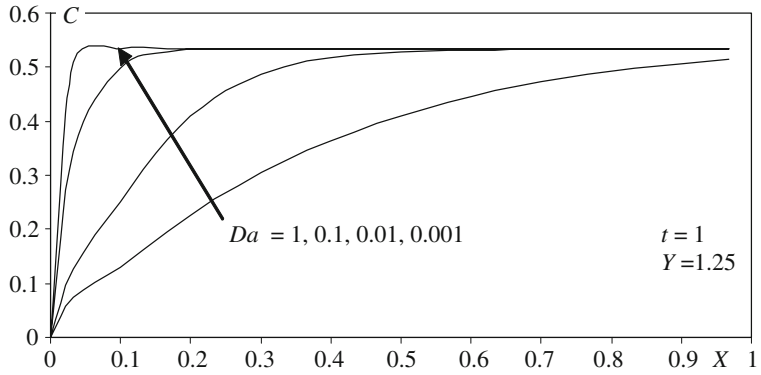

Fig. 27 Transient concentration distribution with X at $Y = 1.25$ and $t = 1$ for various values of Da

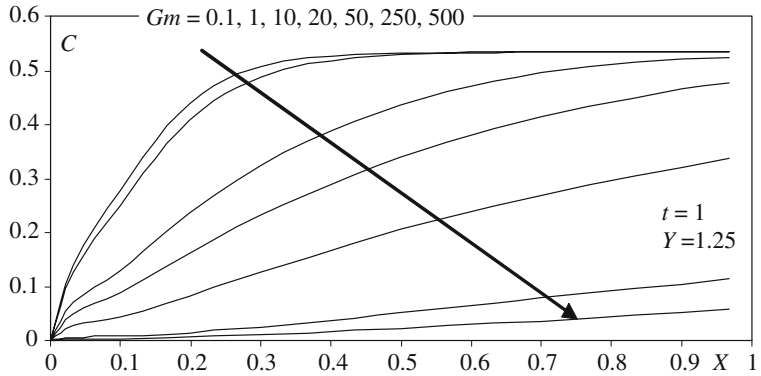

Fig. 28 Transient concentration distribution with X at $Y = 1.25$ and $t = 1$ for various values of Gm

permeable soil, therefore, aids in increasing concentration distribution along the wall, since less contaminant is able to percolate the porous structure and spread more evenly throughout the regime. From Figs. 28, 29 and 30, an increase in Gm (species buoyancy Grashof number), Pr (Prandtl number) and Sc (Schmidt number), concentration function values are seen to, respectively, decrease substantially, increase slightly and decrease strongly.

Figures 31–34 illustrate the distribution of the dimensionless gradient parameters defined in Eqs. (15) to (17), vs. local skin friction (i.e. shear stress function), local Nusselt number and local Sherwood number. In these plots we have studied the interaction of two parameters simultaneously. Shear stress function at the wall, τ_X, is seen to decrease with Gm in Fig. 31. The values for $Fs = 0$ (no inertial drag force, i.e. Darcian case), are slightly greater than for $Fs = 0.1$ since less resistance to the flow is generated in the absence of quadratic porous drag. As expected the local Nusselt number (Fig. 32), Nu_x, decreases with a decrease in the

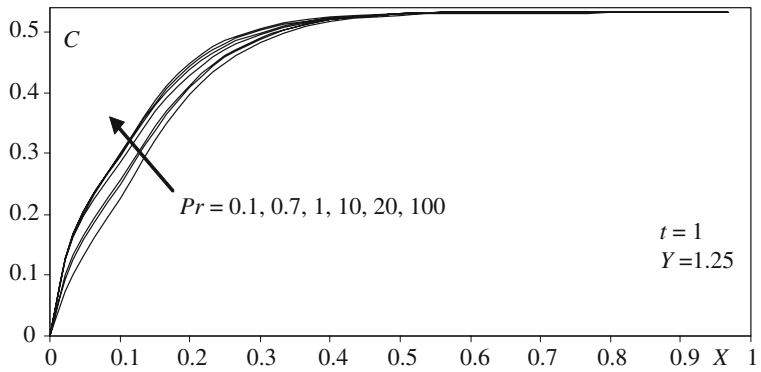

Fig. 29 Transient concentration distribution with X at $Y = 1.25$ and $t = 1$ for various values of Pr

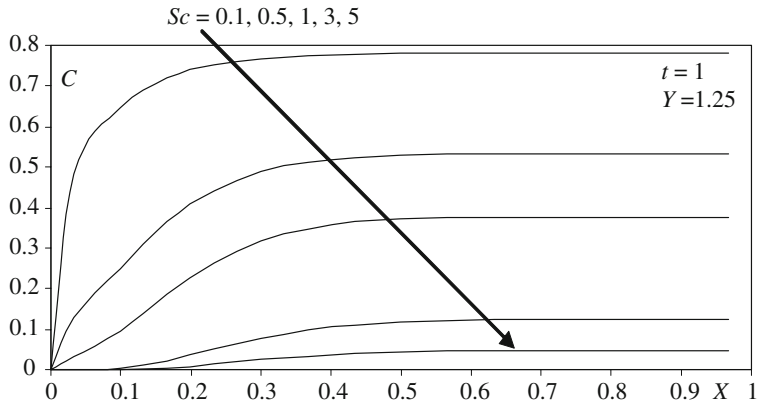

Fig. 30 Transient concentration distribution with X at $Y = 1.25$ and $t = 1$ for various values of Sc

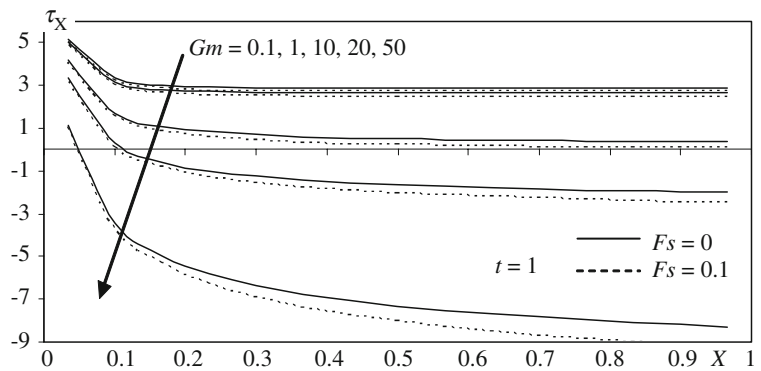

Fig. 31 Transient local skin friction distribution with X at $t = 1$ for various values of Gm and Fs (composite effect of species buoyancy and inertial drag)

Stark number, N, i.e. an increase in thermal radiation heat transfer contribution. There is a minute difference between the Darcian ($Fs = 0$) and non-Darcian ($Fs = 0.1$) cases, where we observe that Nu_x values are fractionally higher for the non-Darcian scenario. Figure 33 shows that a rise in species Grashof number, Gm, induces an increase in Nu_x, i.e. it elevates the heat transfer rate at the wall. The values for the non-Darcian case are slightly lower than the Darcian case ($Fs = 0$). In Fig. 34 we observe the collective influence of species Grashof number and Forchheimer number on the Sh_x distribution with X at $t = 1$. The response is similar to the effect of Gm on Nu_x (Fig. 33) although, as expected, values are higher, since Sh_x is related directly to the *species diffusion* behavior. The non-Darcian values ($Fs = 0.1$) are always lower than the Darcian values ($Fs = 0$), i.e. greater rates of concentration transfer of contaminant occur for lower porous resistance effects.

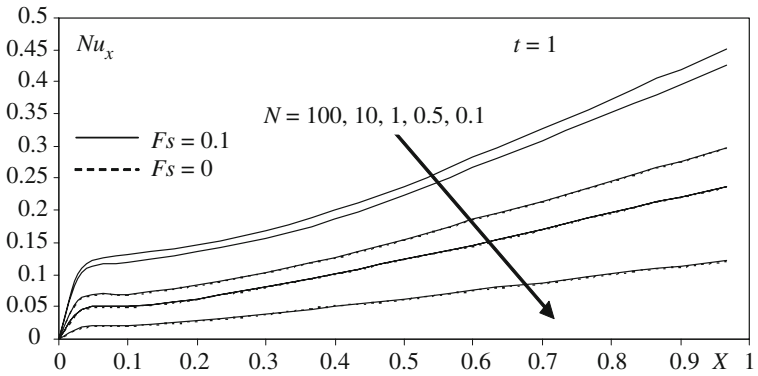

Fig. 32 Local Nusselt number distribution with X at $t = 1$ for various values of N and Fs (combined effect of radiation and inertial drag)

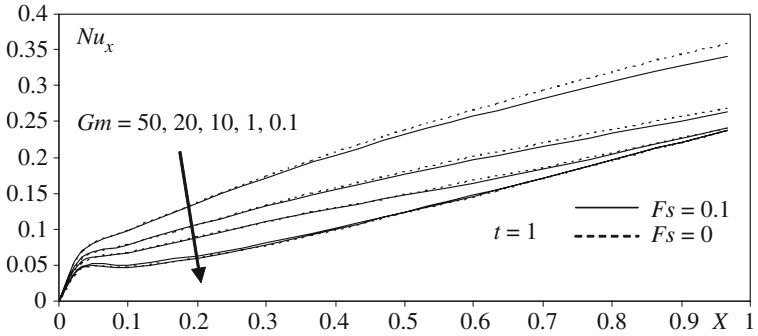

Fig. 33 Local Nusselt number distribution with X at $t = 1$ for various values of Gm and Fs (combined effect of species buoyancy and inertial drag)

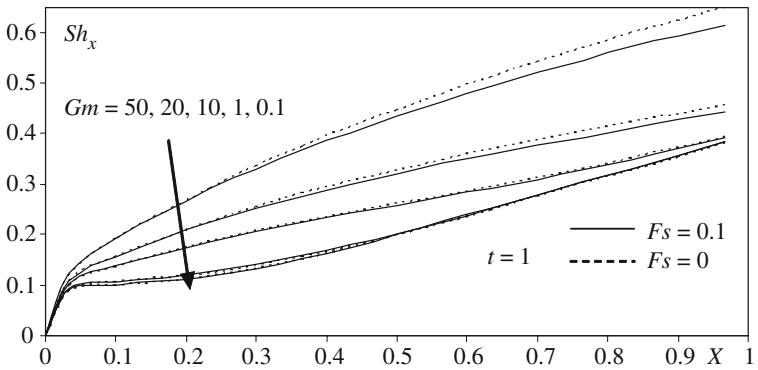

Fig. 34 Local Sherwood number distribution with X at $t = 1$ for various values of Gm and Fs

All the figures discussed thus far have simulated snapshots in time, i.e. *spatial distributions* of different variables, for a *fixed* t value ($t = 1$). In Figs. 35, 36, 37, 38, 39 and 40 we now analyze the variation of transient velocity, U, temperature, T and also concentration, C, *with the time variable,* t, at *fixed points in* X–Y *space*. We observe that transient X-direction velocity (parallel to the wall) increases consistently with a rise in Da throughout time, as shown in Fig. 35. Values rise suddenly for small time and then more gradually until they plateau for the remainder of time. Flow is therefore accelerated for more permeable regimes through time. A decrease in N (Fig. 36) causes a decrease in U values throughout the time domain ($0 < t < 8$). Values shoot up initially due to impulsive nature of the flow for small times and then rise monotonically for the remainder of the t-axis. A decrease in N implies an increase in thermal radiation flux, so that stronger radioactive material accelerates the flow in the geomaterial regime. This is of great importance in monitoring radioactive waste releases in soils adjacent to radioactive waste geo-repositories. The fact that t has small units allows us to

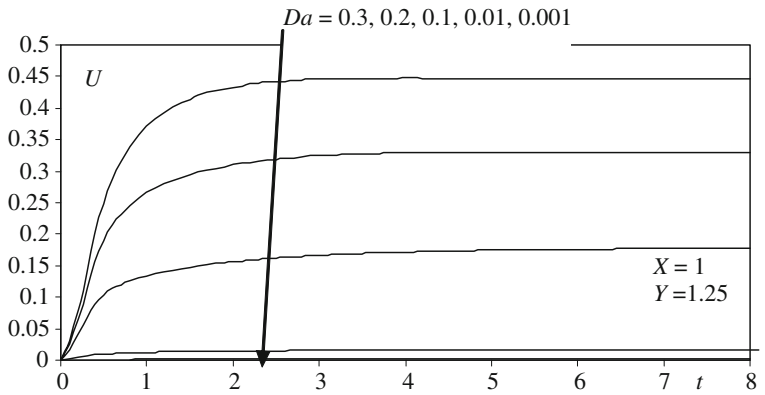

Fig. 35 Transient velocity distribution with time at $X = 1$ and $Y = 1.25$ for various values of Da

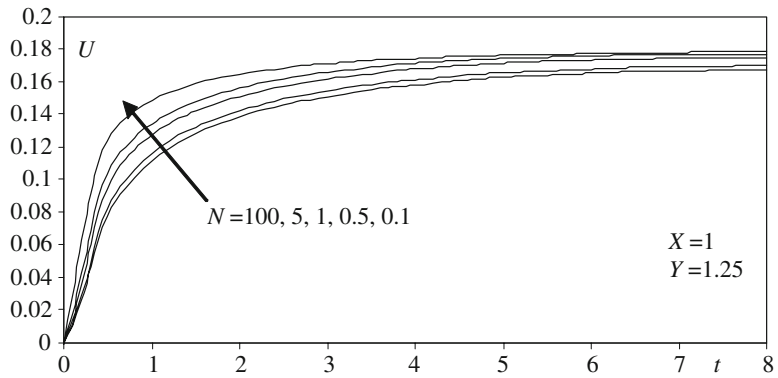

Fig. 36 Transient velocity distribution with time at $X = 1$ and $Y = 1.25$ for various values of N

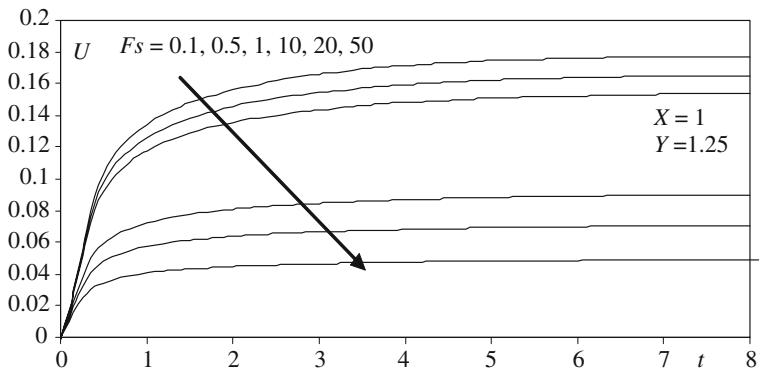

Fig. 37 Transient velocity distribution with time at $X = 1$ and $Y = 1.25$ for various values of Fs

scale the flow in time for different days, months or even years, allowing the prediction of both *short-term* and *long-term* near-field response patterns. Figure 37 depicts the effect of the inertial drag force parameter, Fs on U versus t profiles. As expected, a rise in Fs from 0.1 through to 50, generates greater quadratic porous resistance which consistently decreases the X-direction transient velocity, U, with time. The flow in the geomaterial is therefore strongly decelerated throughout time with an increase in Forchheimer drag.

Figures 38 and 39 illustrate the *temporal distribution* of dimensionless temperature, T, for the respective effects of Da and N. A decrease in Da, i.e. progressively less permeable medium (Fig. 38) induces a marked increase in temperature. With greater fibers in the geomaterial, the conduction heat transfer mode is enhanced boosting the value of temperatures in the regime. A decrease in N (rise in thermal radiation contribution) also serves to increase temperatures (Fig. 39), since the thermal conduction of the fluid is now supplemented by a radiation contribution. Values of T are particularly high in the smaller time frame, i.e. $0.5 < t < 3$.

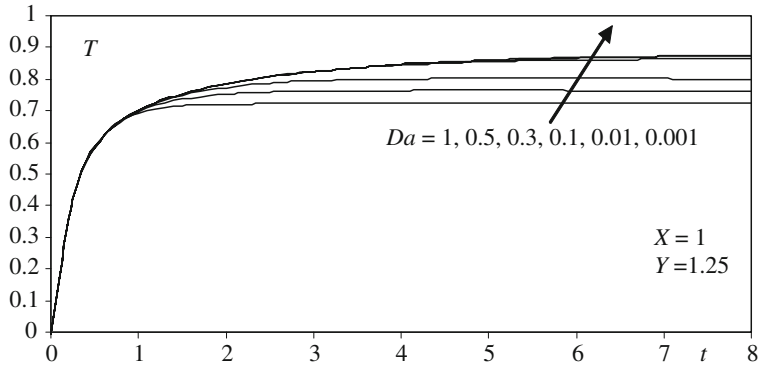

Fig. 38 Transient temperature distribution with time at $X = 1$ and $Y = 1.25$ for various values of Da

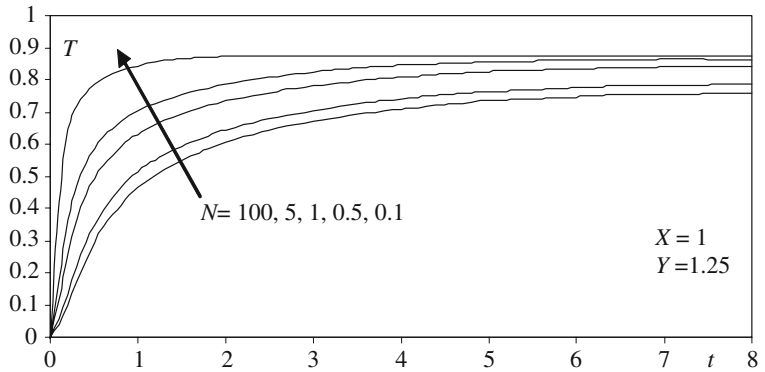

Fig. 39 Transient temperature distribution with time at $X = 1$ and $Y = 1.25$ for various values of N

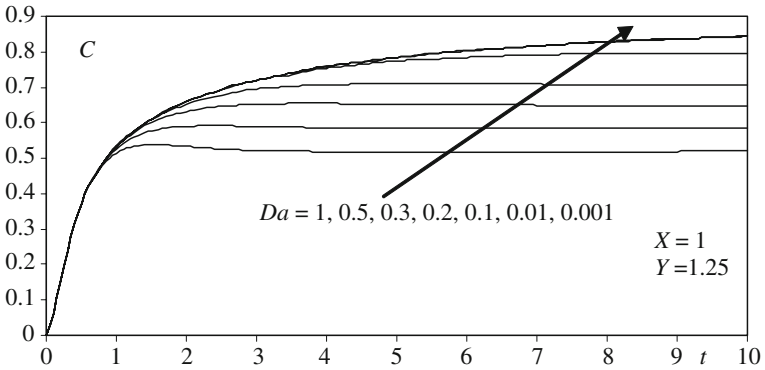

Fig. 40 Transient concentration distribution with time at $X = 1$ and $Y = 1.25$ for various values of Da

Finally, in Fig. 40, we have presented the variation of dimensionless contaminant (species) concentration, C, with time (t) for the influence of Darcy number, Da. A decrease in Da (less permeability) is seen to boost concentration values, i.e. a similar response to transient temperature T is observed for transient concentration. Although further computations were also performed to investigate the effect of increasing Stark number (decreasing thermal radiation contribution from the radioactive contaminant), this was found to have negligible effect on the concentration distribution with time and is therefore not shown here. For small time, negligible effects of increasing Forchheimer number on transient concentration distribution were also found and are again omitted here.

5 Conclusions

A mathematical model has been presented for the time-dependent near-field coupled heat and mass transfer from a radioactive waste material buried in soil, with inertial porous drag effects. Boundary-layer theory is used to derive the transport equations for the heat, mass and momentum transfer in 2D X^*–Y^* space. The partial differential equations of transport are non-dimensionalized and solved, under physically appropriate boundary conditions using a robust numerical method, i.e. NSM. A parametric study of the governing thermo-physical numbers, e.g. Darcy number, Forchheimer number, species Grashof number, etc., is performed. The evolution of velocity, concentration and temperature fields in both space and time is analyzed in detail. Thermal radiation (simulated via the Stark number N) is found to have a strong influence on dimensionless velocities U and V, dimensionless temperature T, but negligible influence on concentration C. An increasing Darcy number is seen to accelerate the flow, while an increase in the Forchheimer number decelerates the flow. The effects of the other parameters are described in detail graphically. The present study finds applications in contamination geomechanics, pollution hydrology and also theoretical modelling of transport phenomena in industrial materials. It is being extended to consider more complex constitutive models for the contaminant (e.g. non-Newtonian models), the results of which will be communicated in the near future.

Acknowledgements The authors wish to thank both reviewers for their excellent comments which have helped to add clarity and enhance the quality of the final manuscript.

References

1. Bear, J., Bachmat, Y.: Introduction to Modelling of Groundwater Pollution. Dordrecht, Netherlands (1987)
2. Bég, O.A.: Advanced Mathematical Modelling in Fire Safety Engineering Science, p 400 (2007, in press)
3. Armstead, H.C.: Geothermal Energy. EN Spon, London (1982)
4. Bég, O.A., Takhar, H.S., Kumari, M.: Computational analysis of coupled radiation convection dissipative flow in a porous medium using the Keller-Box implicit difference scheme. Int. J. Energy Res. **22**, 141–159 (1998)
5. Ingham, D.B., Pop, I. (eds.): Transport Phenomena in Porous Media. Elsevier Science, Oxford (1998)
6. Nield D.A., Bejan A.: Convection in Porous Media. Springer, New York (1992)
7. Bathe, K.J.: Finite Element Procedures. Prentice-Hall, USA (1996)
8. Bég, O.A., Prasad, V., Takhar, H.S., Soundalgekar, V.M.: Thermo-convective flow in an isotropic, homogenous porous medium using Brinkman's model: numerical study. Int. J. Numer. Methods Heat Fluid Flow **8**, 59–89 (1998)
9. Ligget, J.A., Liu, P.L.F.: The Boundary Integral Equation Method for Porous Media Flow. Allen & Unwin, London (1983)
10. Bég, O.A., Bhargava, R., Rawat, S., Takhar, H.S., Bég, T.A.: Finite element modelling of laminar flow of a third grade fluid in a Darcy-Forchheimer porous medium with suction effects. Int. J. Appl. Mech. Eng. **12**(1), 215–233 (2007)
11. Bég, O.A., Takhar, H.S., Bég, T.A., Chamkha, A.J., Nath, G., Majeed, R.: Modelling convection heat transfer in a rotating fluid in a thermally-stratified high-porosity medium: numerical finite difference solutions. Int. J. Fluid Mech. Res. **32**(4), 383–401 (2005)
12. Zueco, J., Alhama, F.: Simultaneous inverse determination of the temperature-dependent thermophysical properties of fluids using the network simulation method. Int. J. Heat Mass Transf. **50**, 3234–3243 (2007)
13. Zueco Jordan, J.: Numerical study of an unsteady free convective magnetohydrodynamic flow of a dissipative fluid along a vertical plate subject to constant heat flux. Int. J. Eng. Sci. **44**, 1380–1393 (2006)
14. Zueco, J.: Unsteady free convection–radiation flow over a vertical wall embedded in a porous medium. Commun. Numer. Method Eng. (in press)
15. Singh, P., Misra, J.K., Narayan, K.A.: Free convection along a vertical wall in a porous medium with periodic permeability variation. Int. J. Numer. Anal. Methods Geomech. **13**(4), 443–450 (1989)
16. Thomas, H.R., Li, C.L.W.: Modelling transient heat and moisture transfer in unsaturated soil using a parallel computing approach. Int. J. Numer. Anal. Methods Geomech. **19**(5), 345–366 (1989)
17. Chen, G.J., Ledesma, A.: Coupled solution of heat and moisture flow in unsaturated clay barriers in a repository geometry. Int. J. Numer. Anal. Methods Geomech. **31**(8), 1045–1065 (2007)
18. Bég, O.A., Bég, T.A., Takhar, H.S., Warke, A.S., Das, S.K.: Mathematical modeling of subsurface contaminant transport with simultaneous first order chemical reaction and second order decay using the ADI scheme. In: HEFAT 2005, 4th International Conference on Heat Transfer, Fluid Mechanics and Thermodynamics, Cairo, Egypt, September (2005)
19. Dybbs, A., Edwards, R.V.: A new look at porous media fluid mechanics: Darcy to turbulent. In: Bear, Corapcioglu (eds.) Fundamentals of Transport Phenomena in Porous Media. NATO Applied Science Series E, pp 199–256. Martinus Nijhoff, The Netherlands (1984)
20. Chamkha, A.J., Takhar, H.S., Bég, O.A.: Numerical modeling of Darcy–Brinkman–Forcheimmer magneto hydro-dynamic mixed convection flow in a porous medium with transpiration and viscous heating. Int. J. Fluid Mech. Res. **29**(1), 1–26 (2002)
21. Skejtne, E., Auriault, J.L.: New insights on steady, nonlinear flow in porous media. Eur. J. Mech. B Fluids **18**, 131–145 (1999)
22. Mei, C.C., Auriault, J.L.: The effect of weak inertia on flow through a porous medium. J. Fluid Mech. **222**, 647–663 (1991)
23. Firdaouss, M., Girermond, J.L., Le Quere, P.: Nonlinear corrections to Darcy's law at low Reynolds numbers. J. Fluid Mech. **343**, 331–350 (1997)

24. Rasoloarijaona, M., Auriault, J.L.: Nonlinear seepage flow through a rigid porous medium. Eur. J. Mech. B Fluids **13**, 1770195 (1994)
25. Lage, J.L.: The fundamental theory of flow through permeable media from Darcy to turbulence. In: Ingham, D.B., Pop, I. (eds.) Transport Phenomena in Porous Media, pp. 1–30. Elsevier Science, Oxford (1998)
26. Kumari, M., Takhar, H.S., Nath, G.: Non-Darcy double-diffusive mixed convection from heated vertical and horizontal plates in saturated porous media. Thermo Fluid Dynamics. Wärme-und Stoffübertragung, vol. 23, pp. 267–273 (1988)
27. Takhar, H.S., Bég, O.A.: Non-Darcy convective boundary layer flow past a semi-infinite vertical plate in saturated porous media. Heat Mass Transf. J. **32**, 33–44 (1996)
28. Bég, O.A., Bhargava, R., Rawat, S., Halim, K., Takhar, H.S.: Computational modeling of biomagnetic micropolar blood flow and heat transfer in a two-dimensional non-Darcian porous medium. Meccanica (2007, in press)
29. Bég, O.A., Zueco, J., Takhar, H.S., Sajid, A.: Transient Couette flow in a rotating non-Darcian porous medium parallel-plate configuration—network simulation method solutions. Acta Mech. (accepted)
30. Siegel, R., Howell, J.R.: Thermal Radiation Heat Transfer, International Student Edition. MacGraw-Hill, New York (1972)
31. Hossain, M.A., Takhar, H.S.: Radiation effects on mixed convection along a vertical plate with uniform surface temperature. Heat Mass Transf. J. **31**, 243–248 (1996)
32. Hossain, M.A., Alim, M.A., Takhar, H.S.: Effects of radiation on mixed convection boundary layer flow along a vertical cylinder. Int. J. Appl. Mech. Eng. **3**, 393–404 (1998)
33. Chamkha, A.J., Takhar, H.S., Beg, O.A.: Radiative free convective non-Newtonian fluid flow past a wedge embedded in a porous medium. Int. J. Fluid Mech. Res. **31**, 101–115 (2004)
34. Domenico, P.A., Schwartz, F.W.: Physical and Chemical Hydrogeology. Wiley, New York (1990)
35. Bear, J.: Dynamics of Fluids in Porous Media. Dover, New York (1988)
36. Bég, O.A., Zueco, J., Takhar, H.S., Bég, T.A., Sajid, A.: Transient non-linear optically-thick radiative–convective double-diffusive boundary layers in Darcian media adjacent to an impulsively started surface: network simulation. Int. J. Nonlinear Mech. (submitted)
37. Raptis, A.: Radiation and free convection flow through a porous medium. Int. Commun. Heat Mass Transf. **25**, 289–295 (1998)
38. Prasad, V.R., Reddy, N.B., Muthucumaraswamy, R.: Radiation and mass transfer effects on two-dimensional flow past an impulsively started infinite vertical plate. Int. J. Thermal Sci. **46**(12), 1251–1258 (2007)
39. Zueco, J.: Network method to study the transient heat transfer problem in a vertical channel with viscous dissipation. Int. Commun. Heat Mass Transf. **33**, 1079–1087 (2006)
40. Pspice 6.0. Microsim Corporation. Irvine, California 92718 (1994)